Hexokinase regulates Mondo-mediated longevity via the PPP and organellar dynamics

Raymond Laboy[1,2], Marjana Ndoci[1], Syed Shamsh Tabrez[1], Maximilian Vonolfen[1,2], Eugen Ballhysa[1,2], Tim Droth[1], Klara Schilling[1,2], Anna Löhrke[1], Ilian Atanassov[1], Adam Antebi[1,2*]

1 Department of Molecular Genetics of Ageing, Max Planck Institute for Biology of Ageing, Cologne, Germany

2 Cologne Excellence Cluster on Cellular Stress Responses in Aging-Associated Diseases (CECAD), University of Cologne, Germany

*For correspondence: aantebi@age.mpg.de

Abstract

The transcriptional complex Mondo/Max-like, MML-1/MXL-2, acts as a convergent transcriptional regulatory output of multiple longevity pathways in *Caenorhabditis elegans*. These transcription factors coordinate nutrient sensing with carbohydrate and lipid metabolism across the evolutionary spectrum. While most studies have focused on the downstream outputs, little is known about the upstream inputs that regulate these transcription factors in a live organism. Here, we found that knockdown of various glucose metabolic enzymes decreases MML-1 localization in the nucleus and identified two hexokinase isozymes, *hxk-1* and *hxk-2,* as the most vigorous regulators of MML-1 function. Upon hexokinase knockdown, MML-1 redistributes to mitochondria and lipid droplets (LD), and concomitantly, transcriptional targets are downregulated and germline longevity is abolished. Further, we found that *hxk-1* regulates MML-1 through mitochondrial β-oxidation, while *hxk-2* regulates MML-1 by modulating the pentose phosphate pathway (PPP) and its coordinated association with lipid droplets. Similarly, inhibition of the PPP rescues mammalian MondoA nuclear translocation and transcriptional function upon starvation. These studies reveal how metabolic signals and organellar communication regulate a key convergent metabolic transcription factor to promote longevity.

Key words: MondoA/ChREBP, MML-1, lipid droplet, metabolism, aging, transcription

Introduction

Aging is a complex multifactorial process associated with organismal homeostasis demise and an increased risk of age-related diseases. One key aspect of aging is the dysregulation of gene expression and metabolism (Fischer et al., 2022). Many transcription factors that regulate metabolic pathways have been shown to control lifespan in the evolutionary spectrum (Clancy et al., 2001; Green et al., 2021; Lapierre et al., 2013; Selman et al., 2008; Wang et al., 2008). Changes in the activity of specific transcription factors have been shown to impact gene expression patterns and alter metabolic processes, leading to a decline in cellular function and an increased risk of age-related diseases (Benhamed et al., 2012; Carroll et al., 2015; Denechaud et al., 2008; Du & Zheng, 2021; Tong et al., 2009). Thus, understanding the interplay between metabolism and transcriptional regulation is crucial for gaining insight into the mechanisms underlying aging and developing novel strategies for promoting healthy aging and reducing the risk of age-related diseases.

MondoA and the Carbohydrate Response Element Binding Protein (ChREBP) are paralogous transcription factors that work in heterodimeric complexes with Max-like protein X (Mlx) and have been identified as key regulators of glucose metabolism and energy homeostasis. These transcription factors recognize and bind hexanucleotide tandem sequences (CANNTG) in the promoter regions called Enhancer box (E-box) sequences (Massari & Murre, 2000) of various genes involved in glucose uptake, utilization, and storage (Billin et al., 2000; Cha-Molstad et al., 2009; Sans et al., 2006; Stoltzman et al., 2008; Yamashita et al., 2001). In addition to their role in glucose metabolism, MondoA/ChREBP have also been shown to regulate lipid metabolism and cellular stress responses (Iizuka et al., 2006; Ishii et al., 2004; Ma et al., 2006). Studies have suggested that changes in MondoA/ChREBP activity with age may contribute to age-related metabolic dysfunction, leading to a decline in glucose tolerance and increased risk of type 2 diabetes and obesity (Ghasemi et al., 2015; Iizuka et al., 2006; Richards et al., 2017; Yamamoto-Imoto et al., 2022).

In *Caenorhabditis elegans,* the transcriptional complex formed by MML-1 (MondoA/ChREBP homolog) and MXL-2 (Mlx homolog) is part of an integrated helix-loop-helix (HLH) network required for lifespan extension in diverse longevity pathways (Johnson et al., 2014; Nakamura et al., 2016). However, how these transcription factors integrate multiple upstream signals to regulate lifespan is still unknown. This work describes how metabolic inputs regulate MML-1 subcellular localization and function. We found that HXK-1 and HXK-2 regulate MML-1 cellular distribution and are required for germline longevity by regulating mitochondrial β-oxidation and the pentose phosphate pathway (PPP), respectively.

68 Moreover, inhibition of MML-1 nuclear translocation results in the relocalization of this
69 transcription factor to mitochondria associated with lipid droplets (LD). This study provides
70 key insights into how glucose and lipid metabolism directly impact transcriptional regulation
71 and aging.
72
73 **Results**
74 *Hexokinases are required for MML-1 subcellular localization and longevity*
75 MondoA reportedly responds to glucose 6-phosphate (G6P) and other hexose
76 phosphate sugars in cultured cells by translocating to the nucleus and regulating the expression
77 of its downstream targets (Stoltzman et al., 2008, 2011). Nevertheless, little is known about
78 MondoA regulation in an organism-wide setting, and most subsequent work has focused on
79 the molecular mechanisms downstream of this transcription factor. Hence, we decided to
80 investigate how MML-1 is regulated by upstream glucose metabolism in *C. elegans*. To
81 address this, we performed a targeted RNA interference (RNAi)-based screen on genes
82 encoding enzymes involved in glucose metabolism. Overall, we found a preponderance of
83 decreased intestinal MML-1 nuclear localization when knocking down such genes (**Figure 1A-**
84 **B, Supplementary Table S1**). Knockdown of most of the enzymes involved in glycolysis, as
85 well as the pyruvate dehydrogenase complex, which links glycolysis to the tricarboxylic acid
86 (TCA) cycle via acetyl-CoA, decreased MML-1 nuclear accumulation (**Supplementary Table**
87 **S1**). Interestingly, whereas most enzymes in the TCA cycle also decreased nuclear MML-1,
88 inhibition of the oxoglutarate dehydrogenase complex (OGDC) subunits *ogdh-1* and *dld-1* and
89 the succinyl-CoA synthase (SCS) *suca-1* and *sucg-1* subunits increased MML-1 nuclear
90 localization. We also observed that knockdown of enzymes involved in the oxidative and
91 nonoxidative branches of the PPP, phosphogluconate dehydrogenase (PGDH) *T25B9.9* and
92 transketolase (TKT) *tkt-1* genes, respectively, triggered a strong increase in MML-1 nuclear
93 accumulation (**Figure 1A-B**). These data suggest that overall changes in glucose metabolism
94 regulate MML-1 and that this transcription factor may sense the divergence of G6P to different
95 branches of this network.
96 Our screen revealed that hexokinase knockdown had the most potent effect in
97 decreasing MML-1 nuclear localization. This enzyme is involved in the first step of glucose
98 metabolism, phosphorylating glucose to G6P, and is a critical mediator of cellular metabolism.
99 Among the three *C. elegans* hexokinase genes, *hxk-1* and *hxk-2* more strongly affected MML-1
100 nuclear localization in two independent MML-1::GFP reporter strains (**Figure 1B,**
101 **Supplementary Figure 1A**), while *hxk-3* had just a small effect on MML-1 nuclear

102 localization, probably due to its low expression in adult worms (Hutter & Suh, 2016). To test
103 whether the phosphotransferase activity of hexokinase is responsible for regulating MML-1
104 nuclear localization, we used two drugs to inhibit hexokinases pharmacologically.
105 3-Bromopyruvate (3-BrP) is an alkylating agent and HKII inhibitor, and 2-deoxy-glucose (2-
106 DG) is an analog of glucose phosphorylated to 2-DG6P, which cannot be further metabolized,
107 thus inhibiting hexokinase function. Supplementation of both drugs significantly decreased
108 MML-1 nuclear localization compared to control (**Supplementary Figure 1B-C**), indicating
109 that hexokinase activity drives MML-1 nuclear translocation. We also tested the specificity of
110 RNAi knockdown by using strains where the three endogenous hexokinase loci were tagged
111 with mKate2. We used these strains to evaluate the protein levels by western blot and found
112 that each RNAi was specific to each isozyme (**Supplementary Figure 1D-E**). As glycolysis
113 is essential during development, we measured the size (area and length) of worms fed with
114 hexokinase RNAi egg-on. *hxk-1i* and *hxk-2i* displayed no significant change in worm growth,
115 while *hxk-3i* treated animals were somewhat smaller (**Supplementary Figure 1F-G**). To
116 determine if our observations were due to a change in food intake, we counted pharyngeal
117 pumping rate but found no significant difference compared to the control (**Supplementary**
118 **Figure 1H**), nor did we see an effect on worm motility compared to control (**Supplementary**
119 **Figure 1I**). Moreover, hexokinase knockdown did not affect the steady-state levels of *mml-1*
120 mRNA (**Supplementary Figure 1J**). Taken together, these data indicate no RNAi cross-
121 reactivity among the hexokinase isozymes and that the effects on MML-1 nuclear localization
122 are not due to a decrease in food consumption or developmental phenotype.
123 MML-1 works in a transcriptional complex with MXL-2, and previous studies have
124 demonstrated that MML-1 and MXL-2 are required for lifespan extension in multiple longevity
125 pathways, including germline-less *glp-1(e2141)* mutant (Nakamura et al., 2016). Hence, we
126 tested whether hexokinases influenced MML-1 subcellular localization in this longevity model.
127 As expected, MML-1 nuclear localization was increased in *glp-1(e2141)* as reported previously
128 (Nakamura et al., 2016), and upon *hxk-1* and *hxk-2* knockdown, MML-1 nuclear localization
129 was abolished in *glp-1(e2141)* mutants (**Figure 1C-D**). Changes in MML-1 nuclear
130 localization would be expected to modulate its transcriptional activity. To test this idea, we
131 next analyzed the expression of downstream targets reportedly linked to gonadal longevity
132 (Nakamura et al., 2016). We observed decreased expression of *mdl-1*, *lgg-2*, *swt-1*, and *fat-5*
133 under *hxk-1i* and *hxk-2i,* but not under *hxk-3i* (**Figure 1E, Supplementary Figure 1K**),
134 consistent with decreased MML-1 transcriptional activity. Since hexokinase knockdown
135 decreases MML-1 nuclear localization in the *glp-1(e2141)* longevity model, we reasoned that

136 the lifespan might also be abolished. Accordingly, *hxk-1i* and *hxk-2i* significantly decreased
137 *glp-1(e2141)* but did not affect wildtype lifespan (**Figure 1F**). These data indicate that
138 hexokinases are upstream regulators of MML-1 nuclear localization and transcriptional
139 function in germline-mediated longevity.
140 Next, we tested whether the effect of hexokinase knockdown on MML-1 nuclear
141 localization and longevity was shared by other longevity pathways. On the one hand, we
142 observed that in *isp-1(qm150)* mutants, a model for mitochondrial longevity, *hxk-1* and *hxk-2*
143 knockdown decreased MML-1 nuclear localization and abolished lifespan extension (**Figure**
144 **1G-H**). On the other hand, while *mml-1* was required for the insulin signaling *daf-2(e1370)*
145 mutant longevity, *hxk-1* and *hxk-2* knockdown did not alter MML-1 nuclear localization nor
146 suppress the lifespan in this background (**Supplementary Figure 1L-M**). Further, we found
147 that MML-1 nuclear localization was increased in *raga-1(ok701)* mutants, a model for
148 mTORC1 longevity, and *mml-1* was required for lifespan extension (**Supplementary Figure**
149 **1N-O**). However, *hxk-1* and *hxk-2* knockdown did not suppress *raga-1(ok701)* longevity
150 (**Supplementary Figure 1P**). Collectively, these data suggest that while MML-1 acts as a
151 convergent factor in these four longevity pathways, it only requires HXK-1 and HXK-2 for
152 germline and mitochondrial longevity, but not for insulin and mTOR longevity.
153
154 *C. elegans hexokinases are differentially expressed*
155 Mammals harbor four hexokinases that differ in tissue expression, subcellular
156 localization, and affinity to glucose and G6P. However, knowledge of the worm isozymes is
157 limited. We used the hexokinase tagged with mKate2 strains to investigate the tissue-specific
158 expression and subcellular localization of the different isozymes by confocal microscopy. We
159 found that HXK-1 was expressed in the cytosol of neurons, pharynx, gonadal sheath, and
160 coelomocytes (**Figure 2A**). HXK-2 had a reticular expression pattern in neurons, muscle,
161 intestine, and hypodermis (**Figure 2B**). HXK-3 signal was diffused and highly expressed in
162 the pharynx, muscle, hypodermis, and intestine (**Supplementary Figure 2A**).
163 Human HKI and HKII have been shown to bind reversibly to the mitochondria (Sui &
164 Wilson, 1997). Binding depends on an intrinsic hydrophobic N-terminal sequence critical for
165 inserting into the outer mitochondrial membrane (Pastorino et al., 2002). Due to the reticular
166 expression pattern, HXK-2 was a plausible candidate to be mitochondrially localized. To
167 corroborate this idea, we crossed the HXK-2::mKate2 strain with a mitochondrial reporter that
168 expresses GFP with a mitochondrial targeting sequence under the body wall muscle promoter
169 *myo-3.* Indeed, we observed that full-length HXK-2 strongly co-localized with mitochondria

170 (**Figure 2C**). We also generated an HXK-2 mutant that lacks the first ten amino acids after the
171 initiator methionine (d10 HXK-2) and found that mitochondrial localization was abolished
172 entirely (**Figure 2C**). In summary, we found that hexokinases are differentially expressed in
173 *C. elegans* and identified HXK-2 as the worm mitochondrial hexokinase.
174
175 *Hexokinase knockdown increases MML-1 mitochondrial localization*
176 Since we observed that *mml-1* mRNA levels were unaffected by *hxk* knockdown and
177 saw a decrease in MML-1 nuclear localization upon hexokinase knockdown, we wondered
178 whether MML-1 might re-localize to another subcellular compartment. First, we crossed the
179 MML-1::GFP reporter strain with two compartmental markers and examined colocalization by
180 confocal microscopy. We looked at the lysosome/endosome reporter strain LMP-1::mKate2
181 but saw no evident colocalization in intestinal cells upon *hxk-2* knockdown or control
182 conditions (**Supplementary Figure 2B-C**). We had previously shown that MML-1 localizes
183 with mitochondria in the hypodermis (Nakamura et al., 2016); however, mitochondrial
184 subcellular localization in other tissues had not been examined. Hence, we crossed the
185 MML-1::GFP strain with the mitochondrial reporter TOMM-20::mCherry under the intestinal
186 promoter *ges-1* and confirmed that MML-1 localized with mitochondria in the intestine
187 (**Figure 2D-E**). Under normal conditions, around 60-80% of the total MML-1 was nuclear, and
188 15% co-localized with mitochondria. Interestingly, MML-1 mitochondrial localization was
189 increased to ~62% of total MML-1 upon *hxk-2i* (**Figure 2F**). Taken together, our data indicate
190 that upon *hxk-2* knockdown, MML-1 is excluded from the nucleus and re-localizes to a subset
191 population of mitochondria.
192
193 *Inhibition of mitochondrial β-oxidation rescues MML-1 nuclear localization under hxk-1i*
194 Many genes that regulate MML-1 localization are involved in mitochondrial
195 metabolism, such as OGDC and SCS, and inhibiting these complexes could activate stress
196 response pathways. Hence, we assessed whether MML-1 nuclear localization was associated
197 with the activation of mitochondrial stress response and oxidative stress. As expected, we
198 observed increased expression of *hsp-6*::*GFP*, a reporter for mitochondrial stress, upon
199 knockdown of mitochondrial components *ogdh-1*, *sucl-1*, and *sucl-2* as well as in control
200 worms treated with antimycin A (AA), a complex III inhibitor (**Supplementary Figure 2D**).
201 However, inducing mitochondrial stress with AA did not affect MML-1 nuclear localization
202 under control conditions and *hxk-2* knockdown (**Supplementary Figure 2E**). Next, we sought

203 to test whether an increase in oxidative stress affects MML-1 nuclear localization. We exposed
204 worms to the ROS-generating compound paraquat and observed induction of the oxidative
205 reporter *gst-4p*::GFP (**Supplementary Figure 2F**); however, we did not see any effect on
206 MML-1 nuclear localization at the concentrations tested (**Supplementary Figure 2G**). Taken
207 together, these data indicate that MML-1 regulation by glucose metabolism genes is
208 independent of mitochondrial and oxidative stress.

209 Hexokinase downregulation might be expected to cause a reduction in the reliance on
210 glycolysis and increase fatty acid metabolism as fuel for cellular maintenance (**Figure 2G**).
211 Mitochondrial β-oxidation is an important pathway that generates acetyl-CoA for the TCA
212 cycle through the catabolism of fatty acids to produce reductants and energy. Hence, we sought
213 to investigate whether decreasing fatty acid oxidation could affect MML-1 nuclear localization
214 upon hexokinase knockdown. First, we measured the neutral lipid content by feeding the
215 worms with the labeled fatty acid C1-BODIPY-C12 and found increased total lipid storage
216 under hexokinase knockdown in the wildtype and *glp-1(e2141)* backgrounds (**Supplementary**
217 **Figure 2H**). Next, we measured the oxygen consumption rate (OCR) upon hexokinase
218 knockdown under basal conditions and with etomoxir supplementation, a mitochondrial
219 β-oxidation inhibitor that acts on the carnitine palmitoyltransferase (CPT). Inhibition of the
220 CPT decreases acyl-CoA import to mitochondria, and changes in OCR are a correlative
221 measure of mitochondrial β-oxidation of fatty acids (Ramachandran et al., 2019). We found no
222 difference in basal OCR under *hxk-1*, *hxk-2*, and *mml-1* knockdown in the wildtype background
223 (**Figure 2H**). *glp-1(e2141)* animals showed decreased basal OCR compared to wildtype,
224 whereas *hxk-1* and *mml-1* knockdown significantly increased the basal OCR compared to *glp-*
225 *1(e2141)* (**Figure 2H**). Interestingly, we saw a greater percentage of OCR reduction upon
226 adding etomoxir under *hxk-1* knockdown in wildtype and *hxk-1*, *hxk-2*, and *mml-1* knockdown
227 in *glp-1(e2141)* (**Figure 2I**), indicating higher mitochondrial β-oxidation levels. We confirmed
228 this result using the transcriptional reporter *acs-2p*::GFP, a mitochondrial acyl-CoA synthase
229 that is induced and required for fatty acid β-oxidation in *C. elegans* (Van Gilst et al., 2005),
230 and found increased expression upon *hxk-1* and *hxk-2* knockdown (**Supplementary Figure**
231 **2I**).

232 We next wondered whether this increase in fatty acid oxidation was responsible for
233 decreased MML-1 nuclear localization under hexokinase knockdown. First, we performed a
234 double knockdown of *hxk-1* or *hxk-2* combined with *acs-2*. MML-1 nuclear localization was
235 rescued upon *acs-2i* under *hxk-1i* (**Figure 2J**). Interestingly, *acs-2i* did not rescue MML-1

236 nuclear localization under *hxk-2i.* We also pharmacologically inhibited fatty acid oxidation by
237 supplementing etomoxir and again saw the rescue of MML-1 nuclear localization under *hxk-*
238 *1i,* but no effect upon *hxk-2i* (**Figure 2K**). These data suggest that HXK-1 normally promotes
239 MML-1 nuclear localization by decreasing mitochondrial β-oxidation and reveal that the two
240 hexokinases might regulate MML-1 nuclear localization through somewhat independent
241 pathways.
242
243 *hxk-2 regulates MML-1 function through increased PPP*
244 G6P can be diverted as a substrate for metabolic pathways other than glycolysis. Thus,
245 we wanted to test whether MML-1 could sense other branches of glucose metabolism. From
246 our RNAi screen, we observed increased MML-1 nuclear localization upon knockdown of two
247 enzymes from the PPP, *T25B9.9* and *tkt-1* (**Figure 1A-B**). The PPP is a cytosolic metabolic
248 pathway involved in the interconversion of 3 to 7-carbon sugars that generate precursors for
249 the biosynthesis of lipids, amino acids, and nucleotides (**Figure 3A**). It also maintains redox
250 homeostasis through NADPH production. To further address these findings, we tested the
251 effect of pharmacological inhibition of the PPP on MML-1 nuclear localization using
252 6-aminonicotinamide (6-AN), which is a competitive inhibitor of the G6P dehydrogenase
253 (G6DH) and phosphogluconate dehydrogenase (6PGD). These two enzymes generate NADPH
254 in the PPP. In agreement with our previous results, we observed increased MML-1 nuclear
255 localization after supplementation with 1 mM of 6-AN (**Figure 3B**). Moreover, we found that
256 *hxk-2i*, but not *hxk-1i*, significantly increased the NADPH levels (**Figure 3C**). Additionally,
257 we found that *hxk-2i* had increased TKT-1 enzymatic activity compared to the control (**Figure**
258 **3D**). These data suggest that inhibition of the mitochondrial hexokinase enhances the PPP.
259 Next, we sought to test the epistatic interaction of hexokinase and PPP knockdown on
260 MML-1 nuclear localization. For these experiments, we performed double RNAi of *hxk-1* and
261 *hxk-2* in combination with the 6PGD *T25B9.9* and transketolase *tkt-1*. Interestingly, knocking
262 down these enzymes rescued MML-1 nuclear localization under *hxk-2i* (**Figure 3E-F**) but did
263 not rescue the localization under *hxk-1i* (**Supplementary Figure 3A**). To evaluate MML-1
264 function, we measured its transcriptional readouts and found that knocking down the PPP under
265 *hxk-2i* rescued the expression of *lgg-2*, *mdl-1*, *swt-1*, and *fat-5* (**Figure 3G, Supplementary**
266 **Figure 3B-D**); however, it had no effect under *hxk-1i* (**Supplementary Figure 3E-H**).
267 Moreover, we observed lower levels of G6P upon double knockdown of hexokinases with
268 *T25B9.9* and *tkt-1* compared to control (**Figure 3H, Supplementary Figure 3I**). Taken

269 together, these data suggest that the PPP activity is increased upon knockdown of the
270 mitochondrial hexokinase HXK-2, and inhibiting the PPP is sufficient to rescue MML-1
271 function independent of G6P levels.

272 Finally, we asked whether reducing the PPP could impact *glp-1(e2141)* lifespan upon
273 *hxk-2* knockdown. Inhibition of the PPP has been reported to extend the lifespan in *C. elegans*
274 by activating the mitochondrial UPR^{mt} (Bennett et al., 2017). As reported previously, we found
275 a significant lifespan extension upon *tkt-1* knockdown in wildtype (**Figure 3I**). Moreover,
276 knockdown of the PPP in the *glp-1(e2141)* background had no additive effect on longevity,
277 suggesting that *glp-1* and *tkt-1i* may share common mechanisms in extending lifespan.
278 Consistent with our data, knockdown of *T25B9.9* and *tkt-1* rescued *glp-1(e2141)* longevity
279 upon *hxk-2i* (**Figure 3I, Supplementary Figure 3J**). Collectively, these data indicate that an
280 increase in the PPP under *hxk-2* knockdown suppresses MML-1 function, and reducing PPP
281 restores longer life, placing PPP epistatically downstream of *hxk-2*.

282

283 *MML-1 interactome uncovers potential regulators of its function and localization*

284 Given the mitochondrial localization of MML-1 and possibly other organelles, we
285 decided to identify potential MML-1 binding partners to better understand its subcellular
286 distribution. We used CRISPR/Cas9 to tag the endogenous MML-1 locus with a 3xFLAG tag.
287 MML-1::3xFLAG was immunoprecipitated from whole-worm lysates, and potential
288 interactors were identified by mass spectrometry. We detected ca.1600 to 2000 different
289 proteins from three biological replicates and observed that the biological replicates clustered
290 together (**Supplementary Figure 4A-B**). We detected several proteins in the
291 immunoprecipitation (IP), including MXL-2, an established MML-1 binding partner (Pickett
292 et al., 2007) (**Figure 4A**). Analysis of the top 50 co-enriched candidates in MML-1 IPs revealed
293 enrichment for nuclear and mitochondrial proteins (**Supplementary Figure 4C**). We also
294 found multiple enriched proteins from different organelles, including lipid droplets (LD).

295 Mitochondria and LD dynamically interact in highly active metabolic tissues, and it has
296 been shown that mitochondria associated with LD have specific metabolic behavior compared
297 to cytosolic mitochondria (*e.g.*, different dynamics, motility, and capacity to burn
298 carbohydrates and lipids) (Gordaliza-Alaguero et al., 2019; Rambold et al., 2015). LD are
299 organelles involved in multiple roles serving as nutrient reservoirs and participating in
300 signaling pathways, and their biogenesis or degradation is tightly coupled to carbohydrate
301 metabolism (**Figure 4B**). Interestingly, PLIN-1, one of the most abundant LD proteins, was
302 co-enriched in MML-1 IP (**Figure 4A**). Hence, we wanted to test whether MML-1 localized to

303 these organelles. First, we used LipiBlue, a dye to specifically visualize LD *in vivo* (Tatenaka
304 et al., 2019), and found that all LipiBlue-stained structures were positive with the LD resident
305 proteins DHS-3::GFP and PLIN-1::mCherry (**Supplementary Figure 4D-F**), indicating that
306 this dye could be used as a reliable method for visualization of LD in *C. elegans*. Next, we
307 examined LipiBlue-stained animals co-expressing MML-1::GFP and TOMM-20::mCherry
308 and saw that MML-1 localized with LipiBlue-positive structures (**Figure 4C**). Interestingly,
309 MML-1 appeared localized to mitochondria associated with LD (**Figure 4C-D**). Moreover, this
310 colocalization was significantly increased upon *hxk-2* knockdown (**Figure 4E**).
311 Inhibition of transaldolase and enzymes from the PPP have been shown to activate a
312 fasting-like response by increasing lipolysis and enhancing the breakdown of LD (Bennett et
313 al., 2017), including higher expression of the adipose triglyceride lipase ATGL-1
314 (**Supplementary Figure 4G**). Therefore, we wondered whether the LD size correlates with
315 MML-1 nuclear localization. We knocked down *hxk-2* and *tkt-1* to decrease and increase
316 MML-1 nuclear localization, respectively. We observed a significant reduction in diameter and
317 the total amount of LDs upon knockdown of *tkt-1*, while *hxk-2i* did not have an effect (**Figure**
318 **4F, Supplementary Figure 4H).** Double knockdown of *hxk-2* and *tkt-1*, however, resulted in
319 smaller and fewer LDs than the control. We also wanted to test whether the HXK-1/fatty acid
320 β-oxidation axis regulation of MML-1 also converged on LD size regulation. Interestingly, we
321 found that knockdown of *acs-2i* and *hxk-1i acs-2i* double knockdown resulted in a mild but
322 significant increase in LD size (**Supplementary Figure 4I)**, supporting the notion that the two
323 hexokinases regulate MML-1 via distinct mechanisms. Collectively, these data suggest that
324 MML-1 can localize with a specific subpopulation of mitochondria associated with LD and
325 that inhibition of the PPP can rescue MML-1 nuclear localization upon *hxk-2i* correlated with
326 decreasing LD size.
327 To test whether LDs directly regulated MML-1 localization, we knocked down *dgat-2*
328 and *atgl-1*, two enzymes involved in LD metabolism. DGAT-2 is a diacylglycerol (DAG)
329 transferase that promotes LD droplet expansion, while ATGL-1 is a rate-limiting enzyme in
330 LD breakdown (**Figure 4B**). First, we measured the neutral lipid composition and found that
331 *atgl-1i* increased lipid levels while *dgat-2i* worms did not show significant changes under *ad*
332 *libitum* conditions (**Supplementary Figure 4J**). Next, we tested MML-1 nuclear localization
333 and observed that *dgat-2i* increased MML-1 nuclear localization while *atgl-1i* resulted in
334 decreased levels of nuclear MML-1 (**Figure 4G**). Finally, we did an epistatic analysis of LD
335 metabolism and the PPP and found that MML-1 nuclear localization in *atgl-1i* was rescued

336 upon *tkt-1* knockdown (**Figure 4H**), thus suggesting that LD metabolism is upstream or parallel
337 to the PPP in MML-1 regulation.
338
339 *The PPP regulates MondoA function in mammalian cells*
340 We next asked whether the PPP regulation of MML-1 we observed in *C. elegans* was
341 conserved in mammals. Specifically, we wanted to determine whether inhibition of the PPP is
342 sufficient to induce MondoA translocation to the nucleus under contrasting conditions where
343 MondoA is mostly cytosolic (starvation media) or split between the nucleus and cytoplasm
344 (high-glucose growing media). To test this, we cultured the HEK293T cells in high-glucose
345 media with 6-AN and subsequently transferred the cells to either high-glucose media or
346 starvation media (**Supplementary Figure 5A**). First, we observed decreased NADPH/NADP+
347 ratio in cells treated with 6-AN and under starvation conditions (**Supplementary Figure 5B**).
348 Next, we found that in both conditions, MondoA nuclear localization was increased upon
349 inhibition of the PPP (**Figure 5A-B**), while there was no evident regulation of MondoA at the
350 transcript level (**Figure 5C**). Consistent with MondoA increased nuclear localization, we
351 observed increased expression of two of the best-described downstream targets of MondoA,
352 *TXNIP* and *ARRDC4* (**Figure 5D, Supplementary Figure 5C**). These findings indicate that
353 the PPP regulates mammalian MondoA localization and transcriptional function.
354
355 **Discussion**
356 Nutrient sensing pathways and metabolism play a central role in modulating aging by
357 establishing resilience and survival metabolic states. Although much work has focused on
358 identifying mediators of these processes, we still know little about how organisms coordinate
359 feedback loops of metabolic pathways and transcriptional responses to establish such states.
360 Here, we present novel carbohydrate and lipid metabolism mechanisms regulating the
361 transcription factor MML-1/Mondo. We observed that MML-1 senses multiple steps of glucose
362 metabolism and found that hexokinases regulate MML-1 function through different
363 mechanisms in *C. elegans*. On the one hand, we found that under *hxk-2* knockdown, MML-1
364 re-localizes to mitochondria and LD, abolishing the longevity of germline-less worms and
365 mutants with reduced mitochondrial function. Moreover, we could rescue MML-1 function by
366 decreasing the PPP independent of the G6P levels. On the other hand, we found that *hxk-1*
367 knockdown decreased MML-1 function by upregulating mitochondrial β-oxidation. Thus, we
368 found two metabolic branches that converge on MML-1 to trigger a transcriptional response

369 and regulate longevity. We note that while MML-1 is required in four different longevity
370 models, namely *glp-1,isp-1, daf-2,* and *raga-1, hxk-1* and *hxk-2* were required only for *glp-1*
371 and *isp-1* mediated longevity. Presumably, the signal transduction wiring is different in *raga-1*
372 and *daf-2*, or their inputs into MML-1 work downstream or in parallel to the hexokinases.
373 MondoA and ChREBP transcription factors have well-established central roles in
374 glucose metabolism (Ma et al., 2006; Sans et al., 2006; Stoltzman et al., 2008; Yamashita et
375 al., 2001), but whether and how glucose metabolic circuits affect Mondo regulation in a whole
376 animal model is little explored. By performing a systematic RNAi-based targeted screen of
377 enzymes involved in glucose anabolism and catabolism, we found that MML-1 senses multiple
378 steps of glucose metabolism in the worm. Among the genes tested, we found MML-1 nuclear
379 localization to be broadly sensitive to the downregulation of glycolytic enzymes, and the
380 knockdown of hexokinase had the most profound effect. Hexokinase carries out the first step
381 in glucose metabolism, the phosphorylation of glucose to form G6P, which can be shunted to
382 multiple metabolic pathways, including glycolysis, the PPP, glycogenesis, and trehalose
383 production. Our findings are consistent with previous work in cultured cells showing that
384 MondoA localization is regulated by HKII, which is thought to stimulate nuclear localization
385 via the production of G6P (Sans et al., 2006). Additionally, MondoA senses other
386 phosphorylated hexoses, including allose and 3-*O*-methylglucose (Stoltzman et al., 2011).

387 Consistent with our genetic findings above, pharmacological inhibition of glycolysis
388 by supplementation with 3-BrP and 2-DG suppressed MML-1 nuclear localization. In contrast
389 to MML-1, MondoA has been shown to accumulate in the nucleus upon 2-DG in rat L6 cells
390 (Stoltzman et al., 2008). A possible explanation for this difference is that our treatment
391 represents a chronic exposure to 2-DG from development until adulthood, while the
392 experiments in cell culture may reflect an acute response. Overall, 2-DG has been used as a
393 glycolytic inhibitor because it can be phosphorylated by hexokinase to 2-DG 6-phosphate;
394 however, it cannot be further metabolized in glycolysis. Further evidence shows that 2-DG not
395 only functions as a catabolic inhibitor but can also be directed to the PPP or other pathways
396 (Chi et al., 1987; Ralser et al., 2008). Moreover, low concentrations of 2-DG have been shown
397 to extend lifespan by restricting glucose metabolism, while higher concentrations of 2-DG and
398 glucose shortened the lifespan in worms (Schulz et al., 2007, Lee et al., 2009), suggesting a
399 threshold for the benefits of glucose metabolism inhibition in lifespan.
400 Additionally, we found an important link between glycolysis and pyruvate metabolism
401 regulating MML-1 localization. Under aerobic conditions, pyruvate is imported into the

402 mitochondria and converted to acetyl-CoA to generate ATP and other reducing molecules.
403 Downregulation of the mitochondrial pyruvate carrier *mpc-1* and the pyruvate dehydrogenase
404 complex (**Supplementary Table S1**) also decreased MML-1 nuclear localization and function.
405 Further, we found MPC-1 enriched in the MML-1 interactome. Interestingly, loss of *MPC1* in
406 yeast has been shown to accumulate pyruvate, lower TCA cycle intermediates, and reduce
407 chronological aging (Bricker et al., 2012; Orlandi et al., 2014). *MPC1* similarly regulates the
408 disposition of glycolytic and TCA intermediates in flies and mammals (Bricker et al., 2012).
409 Pyruvate can also enter the TCA cycle through pyruvate carboxylase PYC-1, which converts
410 pyruvate to oxaloacetate. However, knockdown of *pyc-1* did not affect MML-1 localization
411 (**Supplementary Table S1**), suggesting that MML-1 may sense pyruvate metabolism mainly
412 through oxidative decarboxylation of acetyl-CoA.

413 We also found that MML-1 responds strongly to alterations in the TCA cycle. The TCA
414 cycle allows organisms to oxidize carbohydrates, fatty acids, and amino acids to provide energy
415 and intermediates for the biosynthesis of macromolecules. Interestingly, the knockdown of two
416 subunits of the OGDC, *ogdh-1* and *dld-1*, increased MML-1 nuclear localization. The OGDC
417 is a rate-limiting enzyme within the mitochondrial TCA cycle that decarboxylates
418 2-oxoglutarate to succinyl-CoA. It has been shown that supplementation of 2-oxoglutarate and
419 knockdown of *ogdh-1* extends lifespan through inhibition of ATP synthase, decreasing oxygen
420 consumption, and increasing autophagy in an mTOR-dependent manner (Chin et al., 2014).
421 Whether MML-1 is required for this lifespan extension has yet to be explored. Conceivably,
422 the mitochondrial localization of MML-1 could help sense 2-oxoglutarate levels, and the
423 accumulation of this metabolite could signal translocation to the nucleus. Moreover, glutamine
424 can be converted to glutamate and subsequently to 2-oxoglutarate during glutaminolysis and
425 represents an important mechanism to replenish the TCA cycle under different metabolic
426 challenges. In this case, OGDC plays a pivotal role in channeling anaplerotic reactions into the
427 TCA cycle from glutamine and glutamate and other amino acids that can ultimately be
428 converted to 2-oxoglutarate (*i.e.*, histidine, proline, and arginine) (Owen et al., 2002).
429 Interestingly, increased glutamine-dependent anaplerosis has been shown to regulate MondoA
430 activity in BxPC-3 cells (Kaadige et al., 2009), though the molecular mechanism remains
431 unclear. Whether glutamine, glutamate supplementation, or knockdown of glutamate
432 dehydrogenase can regulate MML-1 nuclear localization remains to be determined.

433 On the other hand, the TCA cycle can operate in reverse to restore TCA intermediate
434 levels (Dalziel & Londesborough, 1968). Increased levels of 2-oxoglutarate due to inhibition
435 of OGDC, or glutamine anaplerosis, can undergo reductive carboxylation by isocitrate

436 dehydrogenase to produce isocitrate. After that, aconitase can convert isocitrate to citrate,
437 which can be exported from the mitochondria for *de novo* lipogenesis. MML-1 could help
438 orchestrate the metabolic rewiring of the TCA cycle with the fatty acid metabolism
439 transcriptional response. Notably, ChREBP has been shown to regulate many lipogenic
440 enzymes, including acetyl-CoA carboxylase (ACC), the fatty acid synthase (FAS), and
441 ATP-citrate lyase (ACLY) (Ishii et al., 2004; Postic et al., 2007). Accordingly, the MML-1
442 transcriptome shows clear regulation of several fatty acid metabolic enzymes (Nakamura et al.,
443 2016).

444 We observed that PPP enzymes strongly influenced MML-1 nuclear localization and
445 function. The PPP is a cytosolic pathway involved in the interconversion of sugars to generate
446 precursors for the biosynthesis of lipids, amino acids, and nucleotides and maintain redox
447 homeostasis. We found that knockdown of PPP components, PGDH *T25B9.9* and transketolase
448 *tkt-1*, enhanced MML-1 nuclear localization, increased the transcription of MML-1 target
449 genes, and restored longevity to *glp-1(e2141)* animals under *hxk-2i*. The PPP is the primary
450 source of NADPH, which plays a vital role in many cellular processes, including fatty acid,
451 nucleotide, neurotransmitter, and cholesterol metabolism, and is an essential reducing agent
452 (Ju et al., 2020). We found that pharmacological inhibition with 6-AN of the two enzymes
453 producing NADPH in the PPP increased MML-1 nuclear localization. We also found increased
454 levels of NADPH and lower levels of G6P under *hxk-2* knockdown. Importantly, these
455 observations suggest that residual G6P may be diverted to the PPP under low mitochondrial
456 hexokinase and further imply that metabolites other than G6P could regulate MML-1 nuclear
457 localization. What this other metabolite could be remains elusive, but a simplifying notion is
458 that MML-1 nuclear localization is promoted by glycolysis or PPP intermediates. Blocking
459 entry into the PPP or TCA might be expected to accumulate such metabolites and promote
460 Mondo nuclear localization. Conversely, depletion of these metabolites would disrupt Mondo
461 nuclear localization and activity.

462 Another possibility is that Mondo organellar distribution is regulated at another scale.
463 Notably, a major output of the PPP and NADPH metabolism is the production of lipids.
464 Interestingly, we found that under *tkt-1* knockdown, fat levels decreased, and LDs were smaller
465 in diameter, suggesting that a reduction in LDs could signal MML-1 to translocate to the
466 nucleus. Consistently, transaldolase *tald-1* knockdown has been shown to increase lifespan and
467 decrease intestinal fat levels in the worm through increased activity of adipose triglyceride
468 lipase ATGL-1 (Bennett et al., 2017). This enzyme is involved in the metabolism of LD under
469 starvation to mobilize stored fats for energy production (Lee et al., 2014).

470 Interestingly, although both HXK-1 and HXK-2 positively regulate MML-1 function,
471 they do so through different mechanisms **(Figure 5E)**. We observed that decreasing the PPP
472 rescued MML-1 nuclear localization and *glp-1* longevity under *hxk-2* knockdown, independent
473 of the G6P levels, but not under *hxk-1* knockdown. Conversely, inhibition of mitochondrial
474 fatty acid β-oxidation is sufficient to rescue MML-1 nuclear localization under *hxk-1*
475 knockdown, but not under *hxk-2* knockdown. Interestingly, *acs-2* knockdown abolished *glp-1*
476 longevity (data not shown), consistent with previous work showing that NHR-49, a
477 transcription factor that drives *acs-2* expression, is required for *glp-1* longevity (Ratnappan et
478 al., 2014). Thus, inhibiting fatty acid β-oxidation promotes MML-1 nuclear localization under
479 *hxk-1i* but abolishes lifespan extension, potentially due to epistatic effects on other
480 transcription factors or processes.
481 How both hexokinases activate different metabolic pathways to regulate MML-1
482 remains unknown and could work at multiple levels. First, there is evidence that differences in
483 the subcellular location of hexokinases may result in the compartmentalization of glucose
484 metabolism, with the channeling of G6P to different pathways (John et al., 2011; Wilson,
485 2003). Mitochondrial hexokinase has preferential access to ATP generated in the mitochondria
486 and provides efficient glycolysis coupling with further pyruvate oxidation by the TCA cycle
487 and oxidative phosphorylation (OXPHOS). Furthermore, mammalian HKI and HKII have a
488 dynamic localization, shuttling between the mitochondrial outer membrane and the cytoplasm
489 (John et al., 2011). Both mammalian hexokinases have been reported to reversibly bind to
490 mitochondria through their N-terminal sequence (Roberts et al., 2014) and via their interaction
491 with VDAC1 (Lindén et al., 1982). This dual localization allows the cell to adapt to different
492 metabolic requirements and maintain energetic balance. Under high levels of G6P, HKII
493 shuttles from the mitochondria to the cytoplasm, causing cells to use glycogen as an energy
494 source (John et al., 2011). The subcellular localization also plays other significant roles in
495 different signaling pathways. For example, mitochondria-bound hexokinase has anti-apoptotic
496 effects (Gottlob et al., 2001), and increased N-acetylglucosamine upon pathogen exposure
497 releases hexokinase from the mitochondria and activates innate immune responses (Wolf et al.,
498 2016). Here we found that *C. elegans* HXK-2 is associated with mitochondria and that this
499 localization is abolished by deleting the first ten amino acids. However, we saw no effect upon
500 *vdac-1* knockdown nor dynamic localization of HXK-2 between mitochondria and cytosol
501 (data not shown). Taken together, these observations suggest that the nematode has dedicated
502 mitochondrial (HXK-2) and cytosolic (HXK-1 and HXK-3) hexokinases.

503 We also found differences in the tissue expression of the different hexokinase isozymes
504 of the nematode: HXK-1 was mainly found in the pharynx, neurons, gonadal sheath, and
505 coelomocytes, while HXK-2 was present in the hypodermis, body wall muscle, and intestine.
506 Consistently, RNAseq data from different tissues in *C. elegans* shows that *hxk-2* is the main
507 isozyme in the body wall muscle and intestine (Hutter & Suh, 2016). At the same time, *hxk-1*
508 is the main one expressed in pharyngeal muscle and neurons. This differential distribution
509 could explain how *hxk-1* and *hxk-2* differentially regulate MML-1 through β-oxidation and
510 PPP pathways. Notably, we scored MML-1 nuclear localization in the intestine in our
511 experiments, where *hxk-2* but not *hxk-1* is expressed. In the future, it will be important to see
512 whether *hxk-1* cell autonomously impacts *mml-1* nuclear localization within the same tissue,
513 such as the pharynx.
514 In any case, our observation that HXK-1 affects intestinal MML-1 nuclear localization
515 suggests cell non-autonomous signaling. What might be the nature of such cell non-
516 autonomous signaling? One possibility is the sterol hormone signaling pathway, which acts in
517 somatic reproductive tissue to regulate *glp-1(e2141)* longevity. Decreasing the activity of the
518 nuclear hormone receptor DAF-12, or its ligands dafachronic acids, abolishes the longevity of
519 germline-less worms (Gerisch et al., 2001; Yamawaki et al., 2010). Interestingly, carbohydrate
520 metabolism directly impacts the production of dafachronic acids as NADPH is required for the
521 last step of dafachronic acid biosynthesis by DAF-9 (Motola et al., 2006; Penkov et al., 2015).
522 Furthermore, DAF-9 is expressed in the somatic gonad (spermatheca) and XXX neurons in
523 adult animals (Gerisch & Antebi, 2004). Conceivably, hexokinase downregulation could affect
524 the production of NADPH and dafachronic acids regulating DAF-12 activity, thereby affecting
525 MML-1 function. It will be interesting to see whether dafachronic acid supplementation can
526 rescue MML-1 nuclear localization upon *hxk-1i* or *hxk-2i*.
527 The nervous system also plays a crucial role in integrating metabolic status and
528 systemic responses in a cell non-autonomous manner (Mutlu et al., 2020; Zhang et al., 2019).
529 Inhibition of the mTOR signaling pathway has been shown to extend lifespan across the
530 evolutionary spectrum (Kennedy & Lamming, 2016), and recent work has shown that restoring
531 *raga-1/*RagA or *rsks-1/*S6K in the nervous system is enough to entirely suppress the lifespan
532 extension conferred by mutation of these mTOR signaling factors (Zhang et al., 2019). In cells,
533 HKII has been shown to shuttle from the mitochondria and directly interact with mTOR under
534 glucose deprivation and inhibit its function resulting in an induction of autophagy (Roberts et
535 al., 2014). This interaction is dependent on the mTOR signaling (TOS) motif present in HKII

536 required for binding to Raptor. Interestingly, this TOS motif (KDIDI) is conserved in the
537 nematode HXK-1; however, HXK-2 and HXK-3 lack this sequence. Our finding that *raga-1*
538 mutants are epistatic to hexokinase knockdown for life span extension is consistent with a role
539 of mTOR signaling downstream of hexokinase. It would be interesting to study whether the
540 interaction between hexokinase and mTOR is conserved in *C. elegans* and whether decreasing
541 the main neuronal hexokinase (HXK-1) would result in mTOR-dependent inhibition of MML-
542 1.

543 Proteins tend to co-localize near their substrates to maximize specificity and regulate
544 signaling pathways. In particular, MondoA was first reported to be associated with the
545 mitochondria outer membrane in primary human SkMC cells through protein-protein
546 interaction (Sans et al., 2006). We have previously shown that this localization is conserved in
547 *C. elegans* (Nakamura et al., 2016). Mitochondria-bound MondoA has been proposed to have
548 preferential access to newly synthesized G6P from HKII to coordinate metabolism and
549 transcriptional response (Wilde et al., 2019). However, the identity of the mitochondrial factor
550 tethering MondoA at the mitochondria remains unknown.

551 Interestingly, our proteomics analysis of MML-1 immunoprecipitation showed
552 enrichment with proteins from different cellular compartments, including mitochondria, ER,
553 LD, and nucleolus, suggesting an important role of Mondo in integrating diverse organellar
554 signals. Localization to mitochondria was particularly conspicuous. Multiple nuclear
555 transcription factors are localized in the mitochondria, although dissecting their nuclear and
556 mitochondrial function is challenging (Leigh-Brown et al., 2010). On the one hand, nuclear
557 transcription factors have been shown to directly bind the mitochondrial genome to regulate
558 transcription, such as the cAMP response element-binding (CREB) protein (Marinov et al.,
559 2014). Interestingly, *mml-1(ok849)* loss-of-function mutants showed a decrease in all 12
560 mitochondrial-encoded genes compared to wildtype (Nakamura et al., 2016). However, this
561 could be indirect by regulating the mitochondrial transcription factor TFAM or mitochondrial
562 biogenesis (Li et al., 2005). On the other hand, transcription factors like p53 have been shown
563 to translocate to the mitochondrial outer membrane under apoptotic signals to interact with
564 Bcl-2 and promote membrane permeabilization and apoptosis (Marchenko et al., 2007). Future
565 studies will help elucidate whether MML-1/MondoA mitochondrial localization regulates
566 other cellular processes independent of its nuclear transcription function.

567 LD represents the main lipid storage in cells to balance metabolism and energy
568 demands. These organelles are essential for many signaling pathways and are required for
569 survival during fasting by mobilizing lipids for energy production. In *C. elegans,* LDs are

570 mainly localized in the intestine and hypodermis and are composed almost exclusively of TAG
571 (Vrablik et al., 2015). We found PLIN-1, one of the most abundant LD proteins, enriched in
572 the MML-1 interactome. Interestingly, we found that MML-1 colocalizes with LD *in vivo* in
573 the intestine. MondoA was previously seen in large-scale proteomics associated with LD
574 (Krahmer et al., 2018). It was shown that MondoA and Mlx localized with LD through
575 amphipathic helices in the C-terminus in SUM159 cells (Mejhert et al., 2020). The researchers
576 proposed a model in which MondoA/Mlx colocalization with LD inhibits its transcriptional
577 activity, limiting glucose-dependent transcription. Work by Brunet and colleagues suggests
578 that MUFA intercalation into LD and peroxisomes somehow promotes longevity, though
579 downstream transcription factors are little explored (Papsdorf et al., 2023). Mitochondria and
580 LD physically interact with one another to regulate metabolism (Boutant et al., 2017). As
581 MondoA has also been shown to localize with mitochondria, it would be interesting to
582 understand the role of this organelle in regulating MondoA's association with LD. Although
583 the proteins involved in these contact sites are just beginning to be uncovered, both
584 PLIN1/PLIN-1 and ACSL1/ACS-13 have been proposed to tether mitochondria and LD
585 (Gordaliza-Alaguero et al., 2019).
586 Mitochondria bound to LD facilitate the coordination of TAG metabolism and fatty
587 acid oxidation. For example, lipases (*e.g.*, ATGL) in the LDs break down TAG to release free
588 fatty acids that can be activated in the mitochondria's outer membrane by ACSL1 to fatty
589 acyl-CoA. This acyl-CoA can be imported into the mitochondria for β-oxidation. We propose
590 a model **(Figure 5E)** in which MML-1 interacts with specific mitochondria associated with LD
591 to orchestrate a transcriptional response depending on fuel utilization. Under normal
592 conditions, glucose stimulates MML-1 translocation to the nucleus to activate the transcription
593 of glycolytic enzymes. In contrast, upon blockage of glycolysis (*e.g.,* hexokinase knockdown),
594 the cell utilizes fatty acids to produce ATP, re-localizing and inhibiting MML-1 at the
595 mitochondria associated with LD.
596
597 **Materials and Methods**
598 *Worm growth and RNAi treatment*
599 *C. elegans* worm strains were grown and maintained on nematode growth medium
600 (NGM) plates seeded with *E. coli* OP50 strain as the primary food source. Worms were grown
601 at 20 °C unless stated otherwise. *glp-1(e2141)* strains were maintained at 15 °C. All worm
602 strains are listed in **Supplementary Table S4**. Worms were synchronized by 4 to 6 h egg lays

603 at 20 °C. For experiments including *glp-1(e2141)*, egg lays were performed at 15 °C, and the
604 eggs were upshifted to 25 °C for 52 to 56 h to induce the germline-less phenotype. After *glp-1*
605 induction, worms were downshifted to 20 °C until the day of analysis or collection.
606 The NGM media for RNAi knockdown was supplemented with 1 mM isopropyl
607 β-1-D-thiogalactopyranoside (IPTG) and 100 μg mL^{-1} ampicillin. The plates were seeded with
608 the RNAi-expressing *E. coli* HT115 (DE3) strain transformed with the L4440 vector from the
609 Ahringer and Vidal libraries (Kamath & Ahringer, 2003; Rual et al., 2004), or cloned for this
610 work. Bacteria containing luciferase RNAi cloned into the L4440 vector were used as controls.
611 Worms were grown on RNAi plates egg-on in all the experiments.
612
613 *Cell culture experiments*
614 HEK293T (ATCC) cells were maintained in DMEM medium 4.5 g/L D-glucose
615 (Gibco) supplemented with 10% FBS (Gibco). Cells were tested for Mycoplasma
616 contamination by sequencing (Eurofins Genomics). For blocking the PPP, cells were
617 supplemented with 16 and 100 μM 6-AN for 24 to 48 h. After, cells were washed and added
618 fresh DMEM medium or transferred to starvation media (NaCl 140 mM, $CaCl_2$ 1 mM, $MgCl_2$
619 1 mM, HEPES pH 7.4 20 mM, BSA 1%) for 6 h. Cells were collected for immunofluorescence,
620 RNA extraction, and metabolite quantification.
621 For addressing MondoA localization, cells were fixed with 4% paraformaldehyde (PFA) for
622 15 min at room temperature. Following fixation, the samples were washed 3 times with 500
623 μL DPBS, followed by 500 μL of methanol 99% for 5 min at -20 °C, and washed twice with
624 500 μL of DPBS and three times with TBST 1X. Cells were blocked with 10% goat serum
625 diluted in DPBS for 1 h at room temperature. Cells were incubated with 200 μL of the Anti-
626 MondoA antibody (Bethyl Laboratories, A303-195A) 1:500 diluted in goat serum overnight at
627 4 °C. Next, cells were washed 3 times with DPBS containing Triton x-100 (PBST) and
628 similarly incubated with 200 μL of Alexa-488 secondary antibody (Invitrogen, A21206) 1:500
629 diluted in the goat serum at room temperature and covered in aluminum foil for 2 h. After
630 washing 3 times with 500 μL of PBST, the samples were covered with a mounting medium
631 containing DAPI. The cells were cured for 24 h at room temperature in the dark and then stored
632 at 4 °C.
633
634 *Demographic analysis*

635 Lifespan analyses were conducted by synchronizing worms by egg lay. All animals
636 were kept at 20 °C egg on, or transferred to 20 °C on day one of adulthood for the experiments
637 including *glp-1(e2141)*. More than 120 worms were used per strain/condition with 20 to 30
638 worms per 6 cm plate. Worms were transferred every other day to fresh plates until they
639 stopped laying eggs and were scored every time they were transferred. Animals with internal
640 hatching and vulva protrusions were censored from the analysis. All lifespans were performed
641 by blinding the genotypes/RNAi. Demographic parameters like mean, median, and maximum
642 lifespan were calculated and plotted using GraphPad Prism 9 software.
643
644 *Oxygen consumption rate measurements*
645 Oxygen consumption rates (OCR) measurements in *C. elegans* were based on
646 (Koopman et al., 2016). Worms were synchronized by egg lay. 10 to 15 adult worms were
647 transferred to a Seahorse XF96 Cell Culture Microplate (Agilent) with 200 μL of M9 buffer.
648 OCR was measured using the Seahorse XFe96 Analyzer (Agilent). To measure mitochondrial
649 fatty acid β-oxidation, basal oxygen consumption was measured followed by injection of
650 etomoxir (final well concentration 500 μM) and finally injection of sodium azide (final well
651 concentration 40 mM), all measured five times. OCR was normalized to the number of worms
652 with at least six technical replicates.
653
654 *Body measurements, pharyngeal pumping rates, and motility assay*
655 Worms were imaged or recorded using the Leica stereo microscope MDG41 equipped
656 with Leica DFC3000G monochrome camera with a 6.3X magnification. For measuring the
657 body length and area, >20 worms were transferred to a drop of sodium azide 50 mM, imaged,
658 and analyzed in Fiji imaging software. To measure the pharyngeal pumping rates, worms were
659 transferred to a new plate, acclimated on the plates without a lid for 10 min, and then recorded
660 for 30 s. Worm motility was assessed by placing >20 worms in a drop of M9 buffer and
661 recording for 30 s using the Leica M80 Binocular Microscope equipped with the Leica MC170
662 HD camera. Videos were analyzed to count the thrashing of each worm.
663
664 *Molecular cloning*
665 Plasmids were constructed by classical cloning or Gibson Assembly. Restriction
666 enzymes from NEB were used according to the manufacturer's instructions. Custom primers
667 were designed with SnapGene v.5.3.2 and NEBuilder Assembly Tool v.2.5.4 (**Supplementary**

668 **Table S5**). For classical cloning, digested plasmids and amplicons were ligated using the T4
669 DNA Ligase according to the manufacturer's instructions (New England Biolabs). For Gibson
670 Assembly, digested plasmid and amplicon were assembled using NEBuilder HiFi DNA
671 Assembly Master Mix (New England Biolabs) according to the manufacturer's instructions.
672 Plasmids were transformed into *E. coli* DH5α (Life Technologies) strain using the heat shock
673 protocol and plated on LB media supplemented with ampicillin.
674
675 *RNA extraction and RT-qPCR*
676 Worms were synchronized by egg lay for 4 h and collected once they reached the young
677 adult stage in 15 mL conical tubes. The worm pellet was subjected to 4 cycles of freeze and
678 thaw with liquid nitrogen and a water bath at ~37 °C. To lyse the worms, 200 µL of 1.0 mm
679 Zirconia/Silica beads (FisherScientific) were added and transferred to the TissueLyser LT
680 (Qiagen) for 30 min, full speed at 4 °C. Samples were incubated for 5 min at RT. After, 200
681 µL chloroform was added and centrifuged at 12,000 g for 15 min at 4 °C. The top aqueous
682 phase was transferred to a new 1.5 mL tube and mixed with 200 µL of ethanol. The RNA
683 purification was performed using the RNeasy Mini Kit (Qiagen) according to the
684 manufacturer's instructions. The concentration and purity of the RNA samples were quantified
685 using the NanoPhotometer NP80 spectrophotometer (Implen).
686 cDNA was prepared after extracting total RNA from young adult worms or cell extracts
687 using the iScript cDNA Synthesis Kit (BioRad) according to the manufacturer's instructions.
688 Primers, cDNA, and Power SYBR Green Master Mix (Applied Biosystems) were transferred
689 to a 384-well plate using the JANUS automated workstation (PerkinElmer) with four technical
690 replicates per genotype/gene. The reaction was quantified using the ViiA 7 Real-Time PCR
691 system machine (Applied Biosystems). *cdc-42* was used as an endogenous control for the
692 quantification. The complete primer sequences are in **Supplementary Table S5**.
693
694 *Oxidative stress assay*
695 Worms were grown on NGM plates until day 1 adults and then transferred to NGM
696 supplemented with paraquat at 15 and 35 mM for 6 h. As control, we used the CL2166 strain
697 that contains the transcriptional reporter *gst-4p*::GFP. MML-1::GFP nuclear localization was
698 measured in the intestine.
699
700 *Protein extraction and Western blot analysis*

701 Worms were harvested from a mixed population or synchronized by egg lay or
702 bleaching with M9 buffer and washed three times. The worm pellet was snap-frozen in liquid
703 nitrogen and stored at -80 °C until extraction. The pellet was resuspended in liquid lysis buffer
704 supplemented with cOmplete ULTRA EDTA-free protease inhibitors (Roche) and PhosSTOP
705 phosphatase inhibitors (Roche) and sonicated with Bioruptor Plus (Diagenode S.A.) coupled
706 to Minichiller 300 (Huber) for 15 cycles of 30 sec sonication, 30 sec rest at 4 °C. The total
707 protein extract was cleared by spinning down at 20,817 g for 10 min at 4 °C. Supernatant was
708 transferred to a new tube, and protein was quantified using Pierce BCA Protein Assay Kit
709 (ThermoFisher Scientific) according to the manufacturer's instructions. Equal amounts of
710 protein were mixed with 4X loading sample buffer containing DTT 50 mM and boiled at 95
711 °C for 10 min. Samples were loaded onto an SDS-PAGE PERCENTAGE gel (BioRad), and
712 proteins were then transferred onto a nitrocellulose membrane (BioRad) using the Trans-Blot
713 Turbo Transfer System (BioRad). Membranes were blocked for 1 h at RT with 5% milk in
714 TBST. Primary and secondary antibodies were diluted in 5% bovine serum albumin (BSA) in
715 TBST and incubated for 2-18 h at 4 °C. Antibodies: RFP Tag Polyclonal Antibody 1:1000
716 (ThermoFisher Scientific, R10367), Monoclonal ANTI-FLAG M2, Clone M2 1:1000 (Sigma
717 Aldrich, F1804), Anti-beta Actin Antibody 1:1000 (Abcam, Ab8224), Anti-rabbit IgG (H+L)
718 1:5000 (Invitrogen, G21234), Anti-mouse IgG 1:5000 (Invitrogen, G21040), Rabbit Anti-
719 Mouse IgG (Ligh Chain Specific) (D3V2A) mAB (HRP Conjugate) 1:5000 (CST, 58802). The
720 membranes were washed three times with TBST for 10 min at RT in-between incubation with
721 the antibodies and after the secondary. The signals were detected using Western Lightning
722 Plus-ECL, Enhanced Chemiluminescence Substrate (PerkinElmer), and imaged in the
723 ChemiDoc MP Imaging System with Image Lab software (BioRad).
724
725 *Immunoprecipitation*
726 Worms were collected from a mixed population of twenty 10 cm plates, transferred into
727 15 mL conical tubes with M9 buffer, and washed three times. Worms were snap-frozen in
728 liquid nitrogen and stored at -80 °C until extraction. The worm pellet was resuspended in lysis
729 buffer supplemented with cOmplete ULTRA EDTA-free protease inhibitors (Roche) and
730 PhosSTOP phosphatase inhibitors (Roche). Worms were sonicated with Bioruptor Plus
731 (Diagenode S.A.) coupled to Minichiller 300 (Huber) for 30 cycles of 30 sec sonication, 30 sec
732 rest at 4 °C. The total extract was cleared by spinning down at 20,817 g for 15 min at 4 °C.

733 Supernatant was transferred to a new tube, and protein was quantified using Pierce BCA
734 Protein Assay Kit (ThermoFisher Scientific) according to the manufacturer's instructions.
735 The Anti-FLAG M2 magnetic beads (Sigma) were resuspended and equilibrated with
736 TBST buffer. A total of 7 mg of total protein extract in 800 μL was mixed with the magnetic
737 beads and incubated overnight at 4 °C. The next day, the supernatant was removed and stored
738 for WB analysis. The beads were washed 3 times with 1 mL of cold washing buffer #1
739 (Tris/HCl, pH 7.4 20 mM, NaCl 300 mM, EDTA 1 mM, NP-50 0.5%), and 3 times with 1 mL
740 of cold washing buffer #2 (Tris/HCl, pH 7.4 20 mM, NaCl 300 mM, EDTA 1 mM). In the last
741 wash, 500 μL of washing buffer #2 was added, and 100 μL were stored for WB analysis.
742 To elute samples for mass spectrometry, 100 μL of elution buffer (Trypsin 5 ng/μL,
743 Tris/HCl, pH 7.5 50 mM, Tris(2-carboxyethyl)phosphine (TCEP) 1 mM, Chloroacetamide
744 (CAA) 5 mM) were added and incubated for 30 min at RT. The supernatant was transferred to
745 a new 0.5 mL tube and incubated overnight at 37 °C. The next day, formic acid was added to
746 a final concentration of 1% to stop the digestion. Peptides were stored at -20 °C until
747 purification.
748 The peptides were cleaned and purified with StageTip. A 30 μg C18-SD tip was
749 hydrated with 200 μL of methanol, followed by 200 μL of 40% acetonitrile (ACN)/0.1%
750 formic acid (FA). 200 μL of 0.1% FA was added to equilibrate the C18-SD. The digested
751 peptides were dissolved in 0.1% FA and added to the C18-SD and washed once with 0.1% FA.
752 To elute the peptides, 80 μL of 40% ACN/0.1% FA was added, and elutes were collected in
753 0.5 μL tubes and dried in a centrifugal vacuum Concentrator Plus (Eppendorf) for 45 min at
754 45 °C.
755
756 *LC-MS/MS analysis*
757 Peptides were separated on a 25 cm, 75 μm internal diameter PicoFrit analytical column
758 (New Objective) packed with 1.9 μm ReproSil-Pur 120 C18-AQ media (Dr. Maisch) using an
759 EASY-nLC 1200 (ThermoFisher Scientific). The column was maintained at 50 °C. Buffer A
760 and B were 0.1% FA in water and 0.1% FA in 80% CAN, respectively. Peptides were separated
761 on a segmented gradient from 6 to 31% buffer B for 57 min and from 31 to 44% buffer B for
762 5 min at 250 nl/min. Eluting peptides were analyzed on an Orbitrap Fusion Tribrid mass
763 spectrometer (ThermoFisher Scientific). Peptide precursor m/z measurements were carried out
764 at 60,000 resolution in the 350 to 1,500 m/z range. The most intense precursors with charge
765 states from 2 to 7 were selected for HCD fragmentation using 27% normalized collision energy.

766 The cycle time was set to 1 sec. The m/z values of the peptide fragments were measured at a
767 resolution of 50,000 using an AGC target of 2e5 and 86 ms maximum injection time. Upon
768 fragmentation, precursors were put on a dynamic exclusion list for 45 sec.
769 The raw data were analyzed with MaxQuant v.1.6.1.0 (Cox & Mann, 2008). Peptide
770 fragmentation spectra were searched against the canonical and isoform sequences of the *C.*
771 *elegans* reference proteome (proteome ID UP000001940, downloaded December 2018 from
772 UniProt). Methionine oxidation and protein N-terminal acetylation were set as variable
773 modifications; cysteine carbamidomethylation was set as fixed modification. The digestion
774 parameters were set to "specific" and "Trypsin/P". The minimum number of peptides and razor
775 peptides for protein identification was 1; the minimum number of unique peptides was 0.
776 Protein identification was performed at a peptide spectrum match and protein false discovery
777 rate of 0.01. The "second peptide" option was on. Successful identification was transferred
778 between the different raw files using the "Match between runs" option. Label-free
779 quantification (LFQ) (Cox et al., 2014) was performed using an LFQ minimum ratio count of
780 2. LFQ intensities were filtered for at least two valid values in at least one group and imputed
781 from a normal distribution with a width of 0.3 and a downshift of 1.8. Differential expression
782 analysis was performed using *limma* package v.3.34.9 (Ritchie et al., 2015) in R v.3.4.3 (R
783 Core Team, 2017).
784
785 *G6P and $NADP^+$/NADPH measurements and TKT activity assay*
786 G6P and $NADP^+$/NADPH were measured from total worm extracts or cell extracts
787 using the Glucose-6-Phosphate Assay Kit (Sigma MAK014) and the NADP/NADPH-Glo
788 Assay (Promega G9081), respectively, following the manufacturer's instructions. The
789 Transketolase Activity Assay Kit (Fluorometric) (Sigma MAK420) was used to measure TKT
790 activity in worm extracts following the manufacturer's instructions. Samples were normalized
791 to total protein concentration.
792 *glp-1(e2141)* strains were used to avoid signals from the germline. Briefly, worms were
793 synchronized as mentioned previously, collected in a 15 mL conical tube, and washed three
794 times with M9 buffer. Worms were snap-frozen in liquid nitrogen and sonicated using the
795 Bioruptor Plus (Diagenode S.A.) coupled to Minichiller 300 (Huber) for 15 cycles of 30 sec
796 sonication, 30 sec rest at 4 °C. Worms' extracts were cleared by centrifugation at 20,817 g for
797 15 min at 4 °C. Samples were always kept on ice. As mentioned, part of the samples was used
798 to quantify protein, and the rest was used to quantify the metabolites.

799 For G6P colorimetric detection, samples were run in technical duplicates in a 96-well
800 plate. The standard curve was made using the G6P Standard solution provided by diluting with
801 ddH_2O to generate 0 (blank), 2, 4, 6, 8, and 10 nmol/well standards. Samples were combined
802 with the reaction mix in each well and mixed for 30 min at RT, protecting the plate from the
803 light. The absorbance was measured at 450 nm using the POLARstar OMEGA Plate Reader
804 with Luminescence (BGM Labtech). For the analysis, all samples were corrected for the
805 background. The standard curve was generated with the appropriate values obtained by the
806 standards mentioned previously, and the amount of G6P in each sample was calculated with
807 the standard curve. Values were normalized to protein levels.
808 For the $NADP^+$/NADPH bioluminescent assay, samples were run in technical
809 duplicates in a 96-well plate. 50 µL of worm lysis in M9 buffer was incubated with 50 µL base
810 solution with 1% DTAB. Samples were split into two: one to measure $NADP^+$ and the other to
811 measure NADPH. Samples were incubated with or without 25 µL 0.4 N of HCl to measure
812 $NADP^+$ or NADPH, respectively, at 60 °C for 15 min, and then the plate was equilibrated for
813 10 min at RT. Next, 25 µL of Trizma base was added to each well of acid-treated samples to
814 neutralize the acid, and 50 µL of HCl/Trizma solution was added to each well of base-treated
815 samples. An equal amount of the NADP/NADPH-Glo Detection Reagent was added to each
816 well and mixed at RT for 30 min by protecting the plate from the light. The luminescence was
817 recorded using the POLARstar OMEGA Plate Reader with Luminescence (BGM Labtech).
818 Samples were corrected for background luminescence. The relative luminescent units were
819 standardized to the protein concentration.
820
821 *Brightfield and fluorescent imaging*
822 Brightfield and fluorescent images with higher resolution were acquired using the Zeiss
823 Axio Imager Z1 Fluorescent Microscope equipped with the Digital Microscope Camera Axio
824 Cam Mono 506 and the IcC5 true color camera. For fluorescent microscopy, the microscope
825 used a Colibri 7 LED Light Source and the filter sets GFP (Set 38 HE), TR (Set 45), and TL.
826 The software used was Zeiss Zen v2.3.69.1017. Brightfield and fluorescent images were also
827 acquired with the Leica stereo microscope MDG41 equipped with Leica DFC3000G
828 monochrome camera. The microscope was equipped with the Leica EL6000 external light
829 source. The software used was the Leica Application Suite X v3.7.5.24914.
830 All dyes were added to the bacterial lawn, incubated egg on, and protected from the
831 light until the day of imaging. Final solutions were made by diluting in M9 buffer. LipiBlue

832 (Dojindo) was resuspended in 100 µL of DMSO to make a 100 µM stock. The final
833 concentration used was 1 µM. C1-BODIPY-C12 500/510 (ThermoFisher Scientific) was
834 dissolved in DMSO to make a 5 mM stock. The final concentration used was 1 µM. Worms
835 were mounted on a slide with a 5% agarose pad using sodium azide 50 mM. Levamisole 2 mM
836 was used as an anesthetic to image mitochondria.
837 Nuclear localization of MML-1::GFP was quantified in intestinal cells from day one
838 adult worms. Worms were anesthetized with sodium azide 40 mM. At least 20 worms were
839 imaged per genotype/condition. Quantification of the transcription factor nuclear localization
840 was performed by manually selecting each nucleus and calculating the pixel intensity per area.
841 The same area was used to calculate the cytosolic and background signal. Values were
842 corrected by background subtraction. Nuclear localization was calculated by dividing the
843 nuclear signal from the cytosolic signal.
844
845 *Confocal Imaging*
846 Confocal images were acquired with Leica TCS SP8 confocal microscope equipped
847 with a white light laser and a 63X 1.4 NA oil objective. The microscope was also equipped
848 with HyD detectors for fluorescent images and a PMT detector for the bright field. The LAS
849 X Life Science software was used to acquire images and 3D reconstruction. When multiple
850 fluorescent proteins or dyes were imaged, sequential scanning was used to reduce the bleed-
851 through of the signal from one channel to another. All images used for colocalization analysis
852 were deconvoluted with the installed LIGHTNING package to optimize the images and reduce
853 background noise.
854
855 *Statistical analysis and software*
856 The results are presented as mean + SD or SEM, as the figure legends indicate. The
857 number of biological replicates is shown in the figure legends as "N", while the number of
858 worms is presented as "n". Before comparing groups, the data were tested for Gaussian
859 distribution using the Kolmogorov-Smirnov normality test with Dallal-Wilkinson-Lilliefor *p*-
860 value. For normally distributed data, unpaired *t*-test with Welch's correction or one-way
861 ANOVA with Brown-Forsythe and Welch's corrections were calculated in GraphPad Prism 9
862 (GraphPad software). For lifespan analysis, *p*-values were calculated using Log-rank (Mantel-
863 Cox) test. Statistical data from all the lifespans are included in **Supplementary Table S2**.
864 Statistical significance for qPCR experiments was calculated with two-tailed *t*-test. For
865 colocalization analysis, Costes' randomization was performed to determine statistical

866 significance. Significance levels are ns = not significant $p>0.05$, * $p<0.05$, ** $p<0.01$, ***
867 $p<0.001$, **** $p<0.0001$.
868 Image analysis was performed using open-source Fiji package software. Additional
869 JACoP (Bolte & Cordelières, 2006) plugin was used for colocalization analysis. Densitometry
870 analyses were performed using GelAnalyzer v.19.1. Graphs were generated in GraphPad Prism
871 9 and using custom R scripts.
872
873 **Acknowledgments**
874 We would like to thank the CGC (University of Minnesota) and SunyBiotech for some
875 of the strains used in this study. We also thank Katrin Wollenweber and Nadine Hochhard for
876 their technical assistance and the Proteomics, Bioinformatics, and FACS & Imaging Core
877 Facilities at the MPI AGE for their support. Special thanks to Özlem Karalay, Andrea Annibal,
878 Roberto Ripa, Sarah Kreuz, and Victoria Martínez Miguel for the discussions and comments.
879 This work was funded by the Max Planck Society and the Cologne Graduate School for Ageing
880 Research (CGA).
881
882 **Authors contributions**
883 R.L. and A.A. designed the experiments and wrote the manuscript. R.L. performed
884 most of the experiments. M.N. established and performed the MondoA localization upon PPP
885 inhibition in cell culture, S.S.T. performed *hxk-1* lipid droplet and *raga-1* aging experiments;
886 M.V. acquired and processed the samples for proteomics and repeated biological replicates,
887 E.B. measured the $NADPH/NADP^+$ levels in mammalian cells, K.S. carried out *raga-1* aging
888 experiments, I.A. performed proteomic analysis, T.D. and A.L. provided technical assistance.
889
890 **Competing interests**
891 The authors declare no competing interests.
892
893 **Figures**

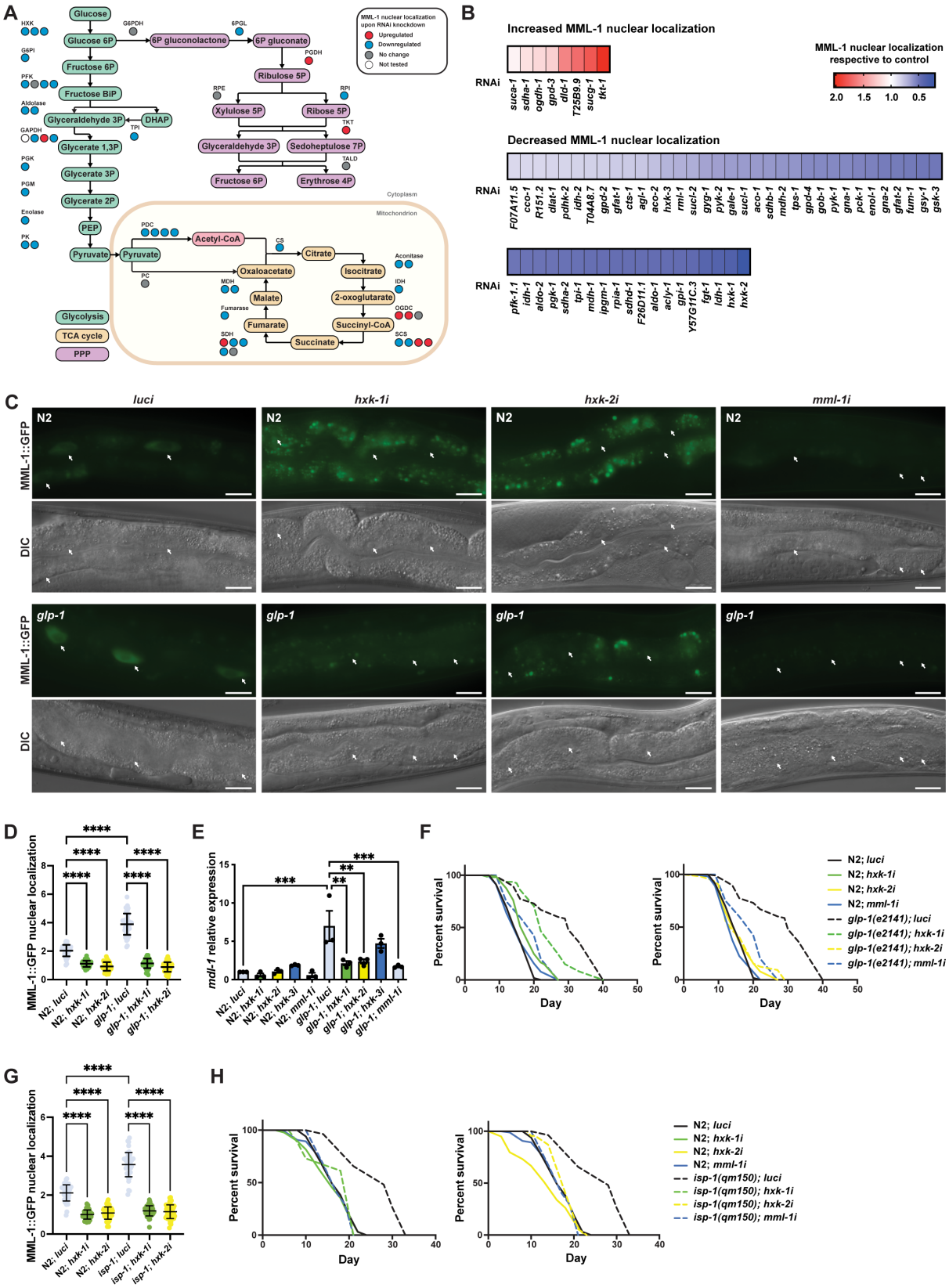

Figure 1. Hexokinases are required for germline longevity by regulating MML-1 localization and function. A. Screening for MML-1 regulators upon knockdown of glucose metabolism enzymes. For clarity, we only mapped the candidate genes involved in glycolysis,

899 the TCA cycle, and PPP. See **Supplementary Table S1** for a complete list of genes tested.
900 MML-1::GFP (dhIs989) nuclear localization was measured in intestinal cells of day one adult
901 worms grown in the RNAi egg-on. Each circle represents one gene encoding an isozyme or
902 subunit of the complex. Circles are color-coded to indicate the increase (red) or decrease (blue)
903 of MML-1::GFP nuclear localization upon knockdown of the enzymes compared to internal
904 *luci* controls. DHAP, dihydroxyacetone phosphate; PEP, phosphoenolpyruvate; TCA cycle,
905 tricarboxylic acid cycle; PPP, pentose phosphate pathway. **B.** Quantification of MML-1 nuclear
906 localization upon knockdown of glucose metabolism genes. Only genes that statistically
907 affected MML-1 nuclear localization compared to the internal *luci* control are depicted
908 ($p<0.05$; $N\geq2$). **C-D.** Representative images (**C**) and quantification (**D**) of MML-1 nuclear
909 localization in wildtype and the germline-less *glp-1(e2141)* longevity background upon
910 knockdown of *luci* (control), *hxk-1i*, *hxk-2i*, and *mml-1i.* MML-1::GFP was quantified in nuclei
911 from intestinal cells (white arrows) in day one adult worms (N=3). Scale bars, 10 μm. **E.**
912 Relative mRNA levels of MML-1 downstream target *mdl-1* in young adult worms measured
913 by qPCR (N=3). **F.** Lifespans of wildtype and *glp-1(e2141)* upon *hxk-1* and *hxk-2* knockdown.
914 Lifespans for *hxk-1* and *hxk-2* knockdown were performed in the same experiment and plotted
915 separately for clarity; therefore, control lifespans are shared between plots. **G.** Quantification
916 of MML-1 nuclear localization in wildtype and *isp-1(qm150)* mutants upon *luci*, *hxk-1i*, and
917 *hxk-2i* in day one adult worms (N=3). **H.** Lifespan of wildtype and *isp-1(qm150)* upon *hxk-1*
918 and *hxk-2* knockdown (N=2). Statistical significance was calculated with *t*-test in **A** and **B,**
919 one-way ANOVA in **D** and **G**, two-tailed *t*-test in **E**, and Log-rank (Mantel-Cox) test in **F** and
920 **H**. **D** and **G** bars represent mean ± SD, and **E** bars represent mean ± SEM.
921

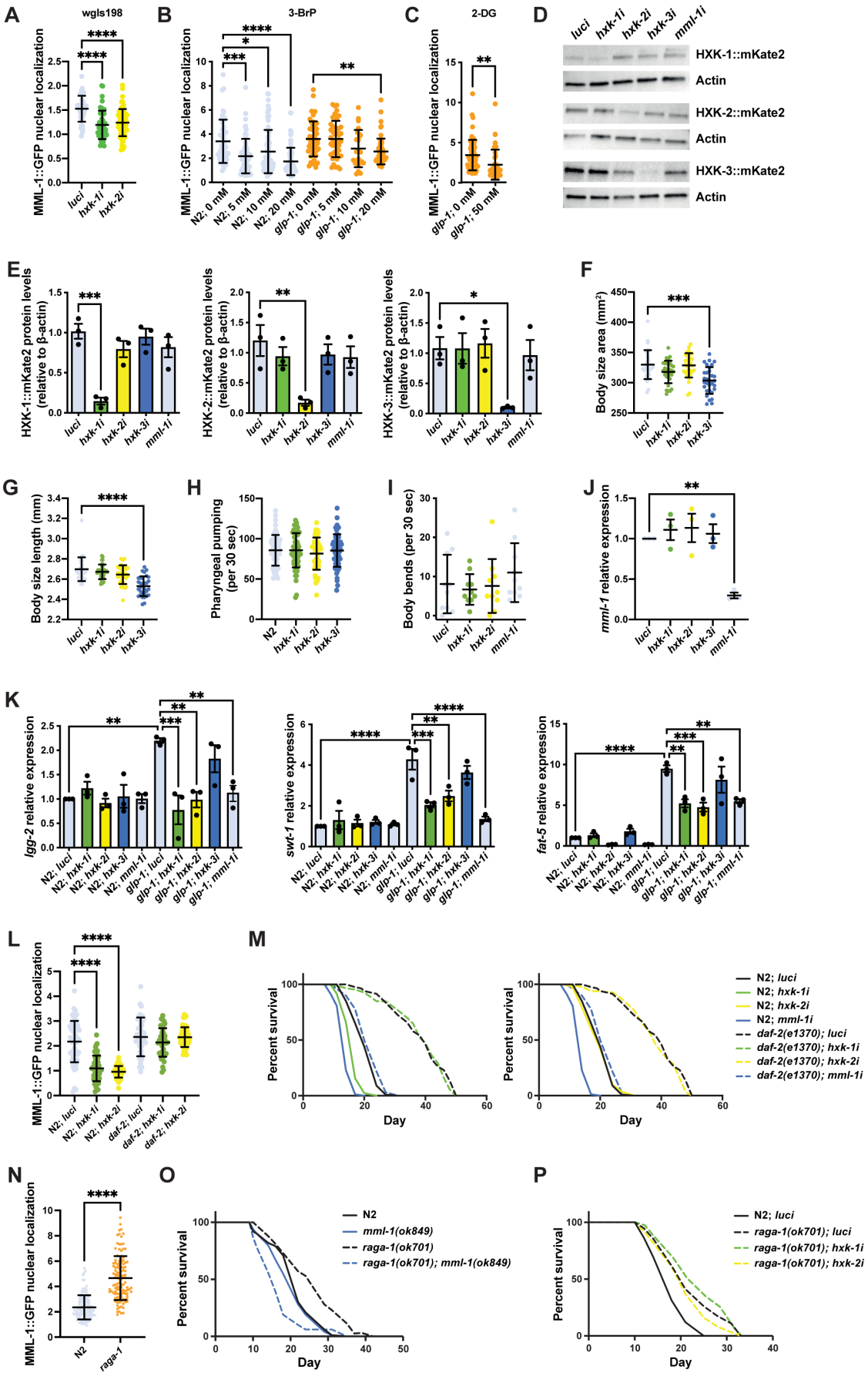
A
wgls198
MML-1::GFP nuclear localization
luci
hxk-1i
hxk-2i
B
3-BrP
N2; 0 mM
N2; 5 mM
N2; 10 mM
N2; 20 mM
glp-1; 0 mM
glp-1; 5 mM
glp-1; 10 mM
glp-1; 20 mM
C
2-DG
glp-1; 0 mM
glp-1; 50 mM
D
luci
hxk-1i
hxk-2i
hxk-3i
mml-1i
HXK-1::mKate2
Actin
HXK-2::mKate2
Actin
HXK-3::mKate2
Actin
E
HXK-1::mKate2 protein levels (relative to β-actin)
HXK-2::mKate2 protein levels (relative to β-actin)
HXK-3::mKate2 protein levels (relative to β-actin)
F
Body size area (mm²)
G
Body size length (mm)
H
Pharyngeal pumping (per 30 sec)
N2
I
Body bends (per 30 sec)
J
mml-1 relative expression
K
lgg-2 relative expression
swt-1 relative expression
fat-5 relative expression
N2; luci
N2; hxk-1i
N2; hxk-2i
N2; hxk-3i
N2; mml-1i
glp-1; luci
glp-1; hxk-1i
glp-1; hxk-2i
glp-1; hxk-3i
glp-1; mml-1i
L
daf-2; luci
daf-2; hxk-1i
daf-2; hxk-2i
M
Percent survival
Day
N2; luci
N2; hxk-1i
N2; hxk-2i
N2; mml-1i
daf-2(e1370); luci
daf-2(e1370); hxk-1i
daf-2(e1370); hxk-2i
daf-2(e1370); mml-1i
N
raga-1
O
N2
mml-1(ok849)
raga-1(ok701)
raga-1(ok701); mml-1(ok849)
P
raga-1(ok701); luci
raga-1(ok701); hxk-1i
raga-1(ok701); hxk-2i

923 **Supplementary Figure 1. Hexokinases regulate MML-1 nuclear localization and**
924 **transcriptional function. A.** MML-1 nuclear localization in the fosmid line wgIs198 was
925 quantified in intestinal cells of day one adult worms using upon *hxk-1* and *hxk-2* knockdown
926 (N=3). **B**. Quantification of MML-1 nuclear localization in intestinal cells of day one adult
927 wildtype and *glp-1(e2141)* worms supplemented with the glycolytic inhibitor 3-bromopyruvate
928 (3-BrP) 5, 10, and 20 mM egg-on (N=2). **C**. Quantification of MML-1 nuclear localization in
929 intestinal cells of day one adult *glp-1(e2141)* worms supplemented with the glycolytic inhibitor
930 2-deoxy-glucose (2-DG) 50 mM egg-on (N=2). **D-E.** Representative Western blot (**D**) and
931 densitometry analysis (**E**) of hexokinases basal levels under *hxk-1i*, *hxk-2i*, *hxk-3i*, and *mml-1i*.
932 Protein levels were normalized to actin as a loading control (N=3). **F-H.** Measurements of body
933 size area (**F**), length (**G**), and pharyngeal pumping rate (**H**) of day one adult worms grown
934 under hexokinase knockdown (N=3). **I**. Motility assay of day one adult worms grown under
935 hexokinase knockdown (N=2). **J.** Relative *mml-1* mRNA levels under hexokinase knockdown
936 measured by qPCR (N=3). **K.** Relative mRNA expression of MML-1 downstream targets
937 *lgg-2*, *swt-1*, and *fat-5* measured by qPCR (N=3). **L.** Quantification of MML-1 nuclear
938 localization in wildtype and *daf-2(e1370)* mutants upon *luci*, *hxk-1i*, and *hxk-2i* in day one
939 adult worms (N=3). **M.** Lifespan of wildtype and *daf-2(e1370)* upon *hxk-1* and *hxk-2*
940 knockdown (N=2). **N.** Quantification of MML-1 nuclear localization in wildtype and *raga-*
941 *1(ok701)* mutants in day one adult worms (N=3). **O.** Lifespan of wildtype, *raga-1(ok701)*, *mml-*
942 *1(ok849)* and *raga-1 mml-1* double mutant (N=3). **P.** Lifespan of wildtype and *raga-1(ok701)*
943 upon *hxk-1* and *hxk-2* knockdown (N=3). Statistical significance was calculated with *t*-test in
944 **C** and **N**, one-way ANOVA in **A-B** and **E-L**, and Log-rank (Mantel-Cox) test in **M** and **O-P**.
945 **A-C**, **F-J**, **L**, and **N** bars represent mean ± SD, and **E** and **K** bars represent mean ± SEM.
946

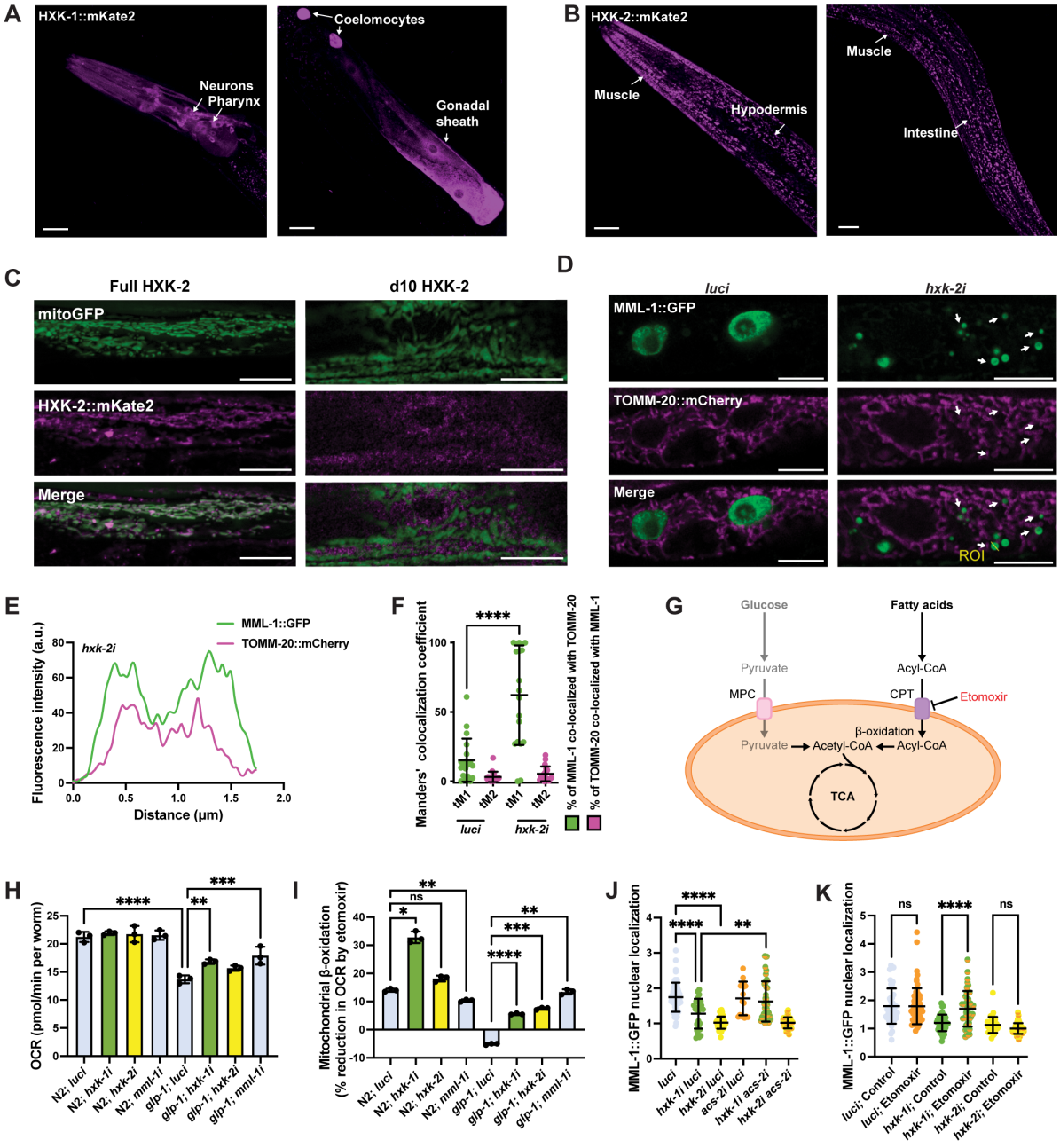

Figure 2. Enhanced mitochondrial β-oxidation suppresses MML-1 nuclear localization upon *hxk-1* knockdown. A-B. Tissue expression of HXK-1::mKate2 (**A**) and HXK-2::mKate2 (**B**) isozymes. The primary tissues are identified with arrows. Scale bars, 20 µm. **C.** Colocalization of mitochondrial reporter *myo-3p*::mitoGFP with full-length HXK-2::mKate2 and d10 HXK-2::mKate2 lacking the first ten residues of the N-terminus. Scale bars, 10 µm. **D.** Representative confocal images of day one adult worms expressing MML-1::GFP and the mitochondrial reporter *ges-1p*::TOMM-20::mCherry under *luci* and *hxk-2i*. Scale bars, 10 µm. **E.** Intensity plot of the region of interest (ROI) from *hxk-2i* (**D**). **F.** Colocalization of MML-1::GFP and TOMM-20::mCherry in *luci* and *hxk-2i*. The colocalization analysis was

958 calculated with the thresholded Manders' colocalization coefficients tM1 (GFP channel) and
959 tM2 (mCherry channel) (N=3). **G.** When glycolysis is reduced, cells rely on fatty acids for
960 energy production. Free fatty acids are activated to acyl-CoA and transported to the
961 mitochondria through the CPT in the mitochondrial outer membrane. The acyl-CoA is then
962 metabolized to generate acetyl-CoA that can enter the TCA cycle to produce energy. MPC,
963 mitochondrial pyruvate carrier; CPT, carnitine palmitoyltransferase. **H-I.** Oxygen consumption
964 rate (OCR) under basal conditions (**H**) and after the addition of the mitochondrial β-oxidation
965 inhibitor etomoxir (**I**). Mitochondrial β-oxidation is calculated as the percentage of decreased
966 OCR after injecting etomoxir (N=3). **J.** MML-1 nuclear localization of day one adult worms
967 grown with double knockdown of *hxk-1* or *hxk-2* combined *acs-2i* (N=3). **K.** MML-1 nuclear
968 localization of day one adult worms grown upon *hxk-1* and *hxk-2* knockdown with
969 supplementation of etomoxir 100 μM egg-on (N=3). Statistical significance was calculated
970 with *t*-test in **F**, and one-way ANOVA in **H-K**. **F** and **J-K** bars represent mean ± SD, **H-I** bars
971 represent mean ± SEM.
972

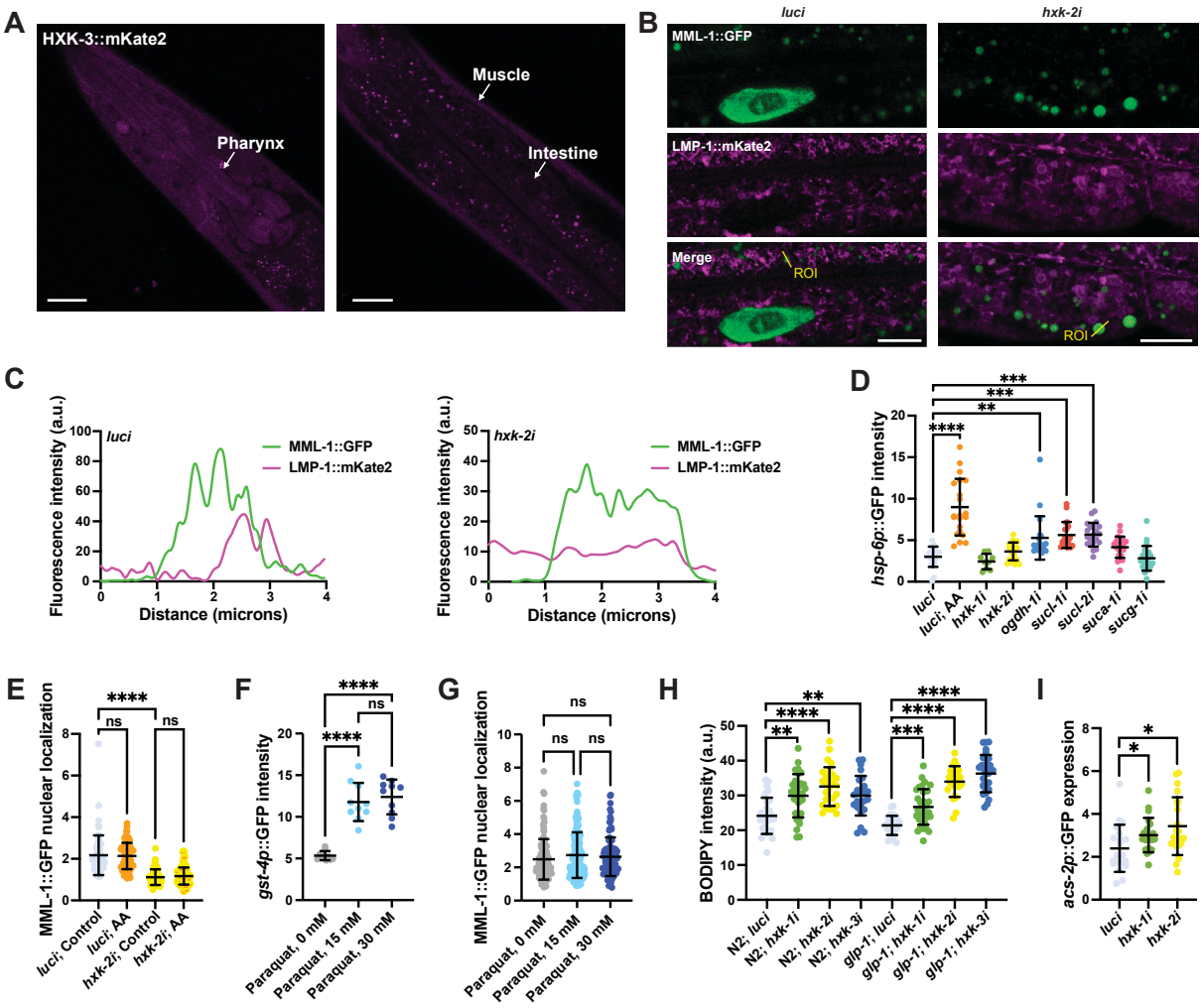

Supplementary Figure 2. MML-1 regulation by glucose metabolism is independent of mitochondrial and oxidative stress response. A. Localization of HXK-3::mKate2 isozyme. The primary tissues are identified with arrows. Scale bars, 20 µm. **B.** Representative confocal images of day one adult worms expressing MML-1::GFP and the lysosome/endosome reporter LMP-1::mKate2 under *luci* and *hxk-2i*. Scale bars, 10 µm. **C.** Intensity plots of the ROIs from **B** (n>10 MML-1 positive puncta per worm). **D.** Quantification of mitochondrial stress response *hsp-6p*::GFP transcriptional reporter upon knockdown of candidate genes regulating MML-1 nuclear localization. Worms were imaged on day one of adulthood. As a positive control for induction of mitochondrial stress, worms were supplemented with antimycin A (AA) 10 µg/mL for 24 h before imaging (N=3). **E.** Quantification of MML-1::GFP nuclear localization of worms grown under *luci* and *hxk-2i* supplemented with AA at the L4 stage, and nuclear localization was measured after 24 h (N=3). **F.** Quantification of day one adult worms expressing *gst-4p*::GFP transcriptional reporter exposed to paraquat for 6 h (N=3). **G.** Quantification of MML-1::GFP nuclear localization of day one adult worms exposed to

989 paraquat for 6 h (N=3). **H.** Neutral lipid content was measured on day one of adulthood by
990 feeding worms with C1-BODIPY-C12 egg-on (N=3). **I.** Quantification of day one adult worms
991 expressing the transcriptional reporter *acs-2p*::GFP under hexokinase knockdown (N=3).
992 Statistical significance was calculated with one-way ANOVA in **D-G**. **D-G** bars represent
993 mean ± SD.
994

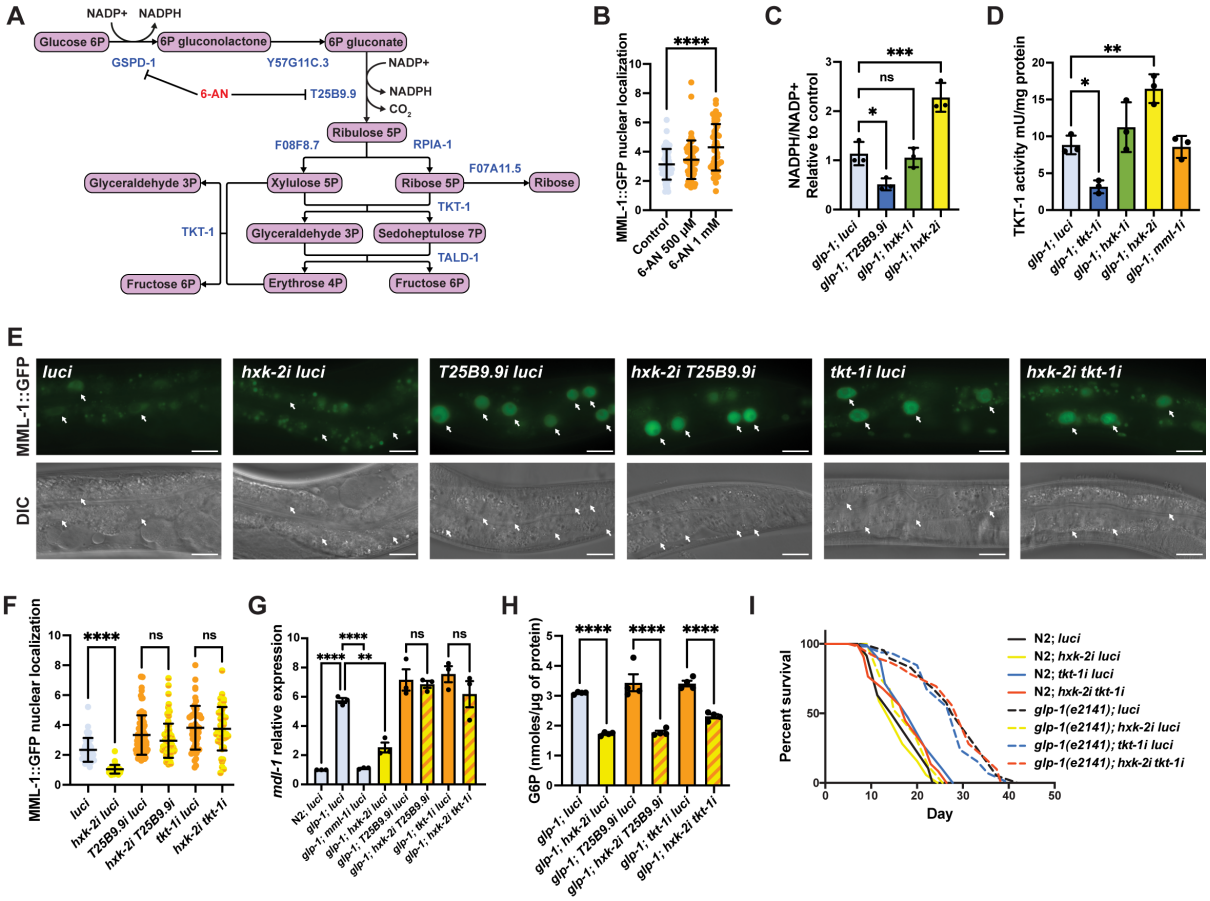

995
996 **Figure 3. HXK-2 regulates MML-1 localization and function through inhibition of the**
997 **PPP. A.** The PPP is a cytosolic pathway that metabolizes G6P to produce NADPH and ribose-
998 5P, and interconverts 3 to 7 carbon sugars. 6-Aminonicotinamide (6-AN) is a PPP inhibitor
999 that acts on the NADPH-producing enzymes GSPD-1 and T25B9.9. **B.** Quantification of
1000 MML-1 nuclear localization of day one adult worms supplemented with 500 µM and 1 mM of
1001 6-AN egg-on (N=3). **C.** Quantification of $NADP^+$ and NADPH levels in day one adult
1002 *glp-1(e2141)* worms grown under hexokinase knockdown. *T25B9.9i* was used as a control.
1003 Metabolite levels were normalized to total protein concentration (N=3). **D.** Transketolase
1004 enzymatic activity assay on day one adult *glp-1(e2141)* worms grown under hexokinase
1005 knockdown. *tkt-1i* was used as a control. Activity levels were normalized to total protein
1006 concentration (N=3). **E-F.** Representative images (**E**) and quantification (**F**) of MML-1 nuclear

localization of day one adult worms upon double knockdown of *hxk-2* with the PPP enzymes *T25B9.9* and *tkt-1* (N=3). Scale bars, 20 µm. **G.** Relative mRNA levels of MML-1 downstream target *mdl-1* in young adult worms upon double knockdown of *hxk-2* in combination with enzymes of the PPP measured by qPCR (N=3). **H.** Quantification of G6P levels relative to total protein measured on day one adult *glp-1(e2141)* upon double knockdown of *hxk-2* in combination with enzymes of the PPP (N=4). **I.** Lifespan analysis of *glp-1(e2141)* with *hxk-2i* and *tkt-1i* single and double knockdowns. Lifespan was performed in the same experiment as **Supplementary Figure 3J**; therefore, control lifespans are shared between plots (N=3). Statistical significance was calculated with a one-way ANOVA test in **B-D** and **F-H**, and Log-rank (Mantel-Cox) test in **I**. **B** and **F** bars represent mean ± SD, **C-D** and **G-H** bars represent mean ± SEM.

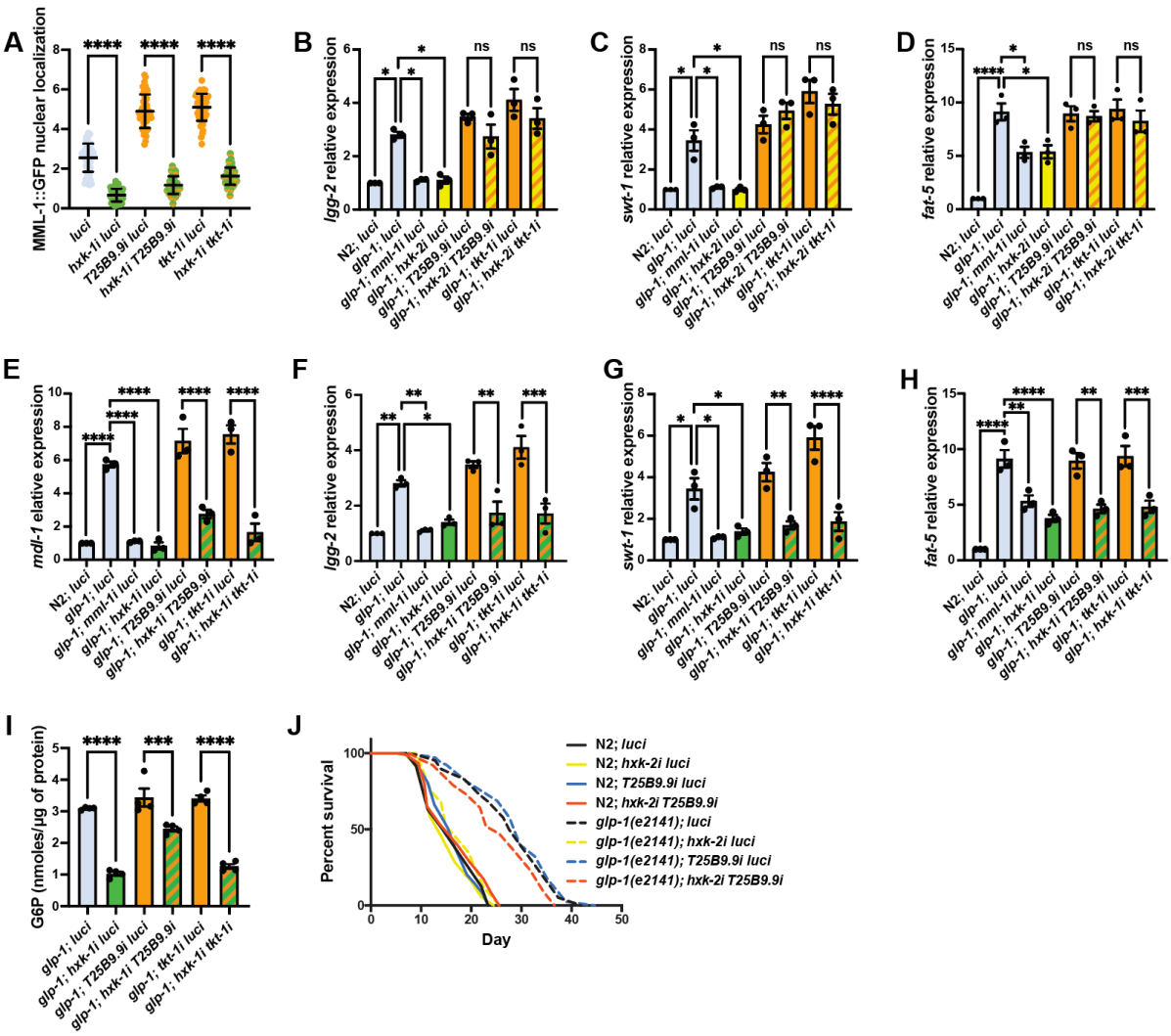

Supplementary Figure 3. HXK-1 and HXK-2 regulate MML-1 through parallel or independent pathways. A. MML-1 nuclear localization of day one adult worms upon double knockdown of *hxk-1* with enzymes of the PPP (N=3). **B-D.** Relative mRNA levels of MML-1 downstream targets *lgg-2* (**B**), *swt-1* (**C**), and *fat-5* (**D**) in young adult worms with double knockdown of *hxk-2* with enzymes of the PPP measured by qPCR (N=3). **E-H.** Relative mRNA levels of MML-1 downstream targets *mdl-1* (**E**), *lgg-2* (**F**), *swt-1* (**G**), and *fat-5* (**H**) in young adult worms with double knockdown of *hxk-1* with enzymes of the PPP measured by qPCR (N=3). **I**. Quantification of G6P levels relative to total protein measured on day one adult *glp-1(e2141)* worms grown under *hxk-1i* in combination with enzymes from the PPP (N=4). **J.** Lifespan analysis of *glp-1(e2141)* with *hxk-2i* and *T25B9.9i* single and double knockdowns. Lifespan was performed in the same experiment as **Figure 3I**; therefore, control lifespans are shared between plots (N=3). Statistical significance was calculated with a one-way ANOVA test in **A-I**, and Log-rank (Mantel-Cox) test in **J**. **A** bars represent mean ± SD, **B-I** bars represent mean ± SEM.

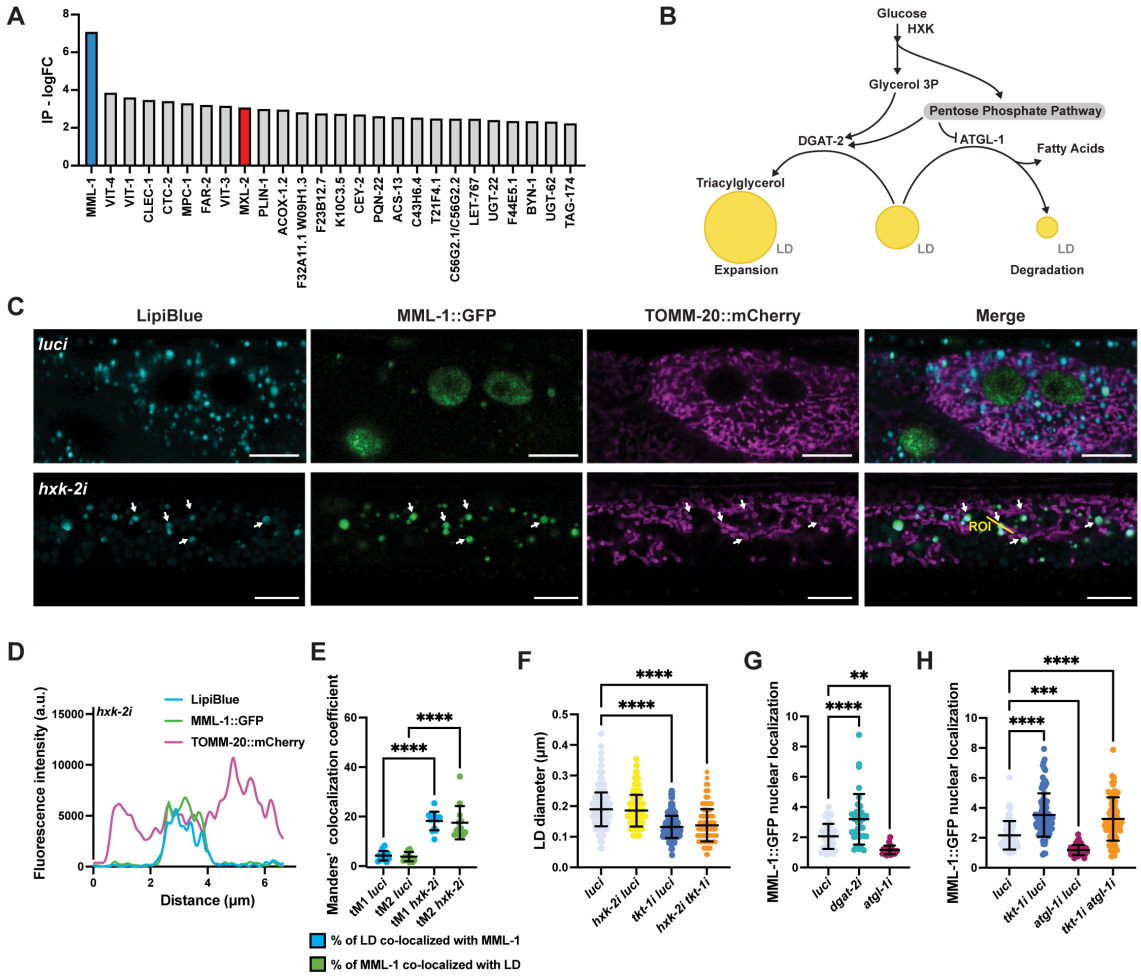

1037 **Figure 4. *hxk-2* knockdown increases MML-1 colocalization with LD. A.** Anti-FLAG
1038 immunoprecipitation (IP) from whole-worm lysates of animals expressing MML-1
1039 endogenously tagged with 3xFLAG in wildtype background. IP was analyzed by mass
1040 spectrometry (LC-MS/MS). The 25 top candidates co-enriched with MML-1 compared to non-
1041 transgenic wildtype control are shown as log FC, including MML-1 (blue) and its established
1042 binding partner MXL-2 (red). **B.** Crosstalk between glycolysis, PPP, and lipid droplet (LD)
1043 metabolism. On the one hand, LD expansion is favored by increased fatty acid synthesis and
1044 subsequent formation of triacylglycerol (TAG) by the diacylglycerol acetyltransferase
1045 DGAT-2. On the other hand, LD consumption releases free fatty acids from TAG by the rate-
1046 limiting lipase ATGL-1. **C.** Confocal microscopy of day one adult worms expressing
1047 MML-1::GFP and the mitochondrial reporter TOMM-20::mCherry stained with the LD dye
1048 LipiBlue under *luci* and *hxk-2i* (N=3). Scale bars, 10 μm. **D.** Intensity plot of the region of
1049 interest (ROI) from *hxk-2i* (**C**). **E.** Colocalization of MML-1::GFP and LD in *luci* and *hxk-2i*.
1050 The colocalization analysis was calculated with the thresholded Manders' colocalization
1051 coefficients tM1 (GFP channel) and tM2 (LipiBlue channel) (N=3). **F.** Quantification of LD
1052 diameter in day one adult worms expressing the LD reporter PLIN-1::mCherry upon
1053 knockdown of *hxk-2* and *tkt-1* (N=3). **G.** Quantification of MML-1 nuclear localization under
1054 knockdown of the LD metabolic enzymes *dgat-2* and *atg-1* (N=3). **H.** Quantification of
1055 MML-1 nuclear localization upon double knockdown of *tkt-1* and *atgl-1* (N=3). Statistical
1056 significance was calculated with a one-way ANOVA test in **E-H**. **E-H** bars represent mean ±
1057 SD.
1058

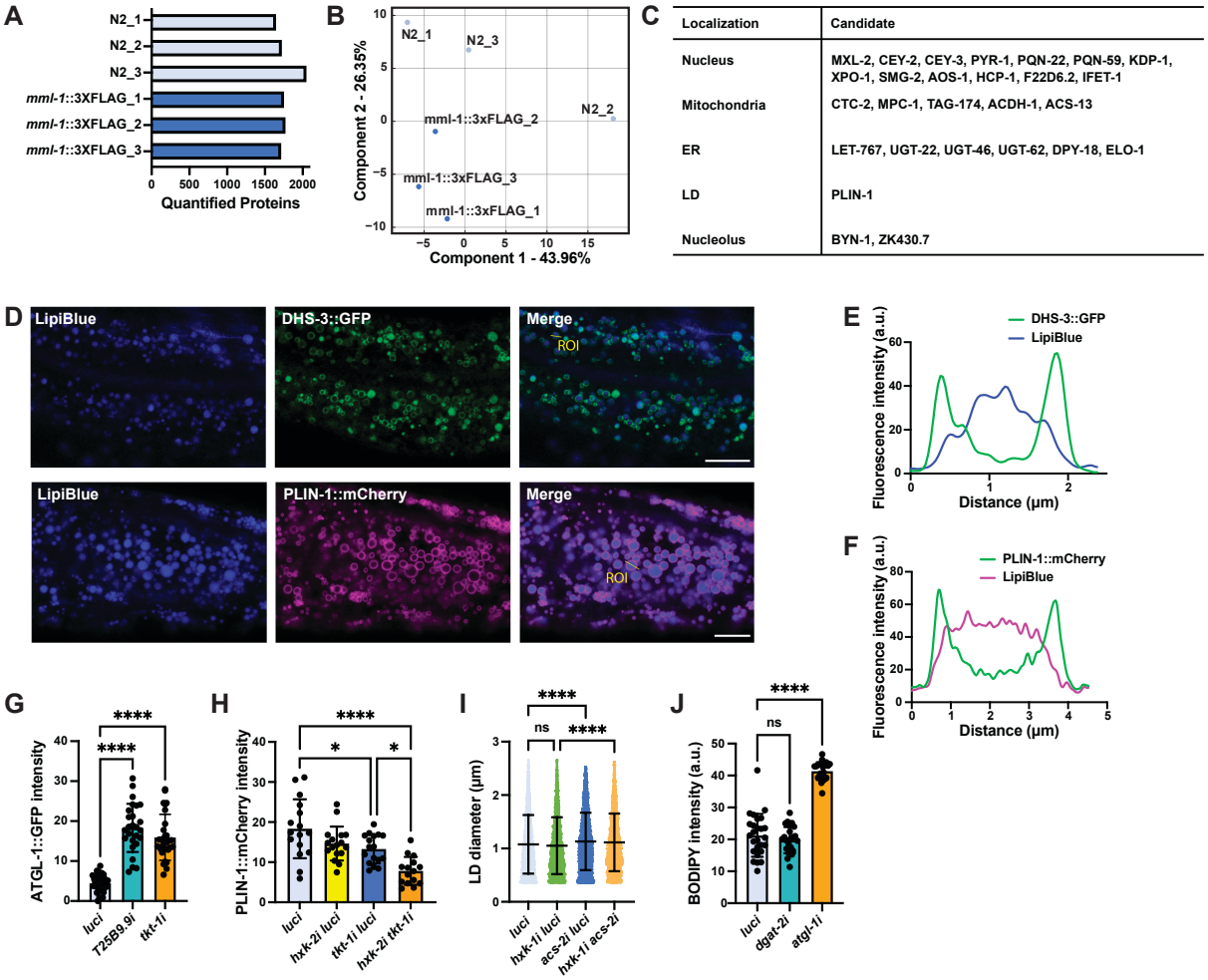

Supplementary Figure 4. MML-1 interactome is enriched with proteins from different organelles. A. Quantified proteins in each biological replicate of wildtype and *mml-1*::*3xFLAG* anti-FLAG immunoprecipitation (IP). **B**. Principal component analysis (PCA) with each biological replicate of the genotypes from proteomics. **C.** Top candidates co-enriched in MML-1::FLAG IP grouped by predicted subcellular localization (uniprot.org). **D.** Representative images of day one adult worms expressing the LD proteins DHS-3::GFP and PLIN-1::mCherry reporters grown with the LD dye LipiBlue egg-on. Scale bars, 10 µm. **E-F.** Intensity plots of the marked ROI from **D** showing DHS-3::GFP (**E**) and PLIN-1::mCherry (**F**) colocalization with LipiBlue. **G.** Expression of the ATGL-1::GFP translational reporter measured on day one adult worms grown under *T25B9.9* and *tkt-1* RNAi egg-on (N=3). **H.** Quantification of LD reporter PLIN-1::mCherry intensity in day one adult worms upon knockdown of *hxk-2* and *tkt-1* (N=3). **I.** Quantification of LD diameter in day one adult worms expressing the LD reporter PLIN-1::mCherry upon knockdown of *hxk-1* and *acs-2* (N=3). **J.** Quantification of neutral lipid content in day one adult worms supplemented with

C1-BODIPY-C12 egg-on under *dgat-2* and *atgl-1* knockdown (N=3). Statistical significance was calculated with a one-way ANOVA test in **G-J**. **G-J** bars represent mean ± SD.

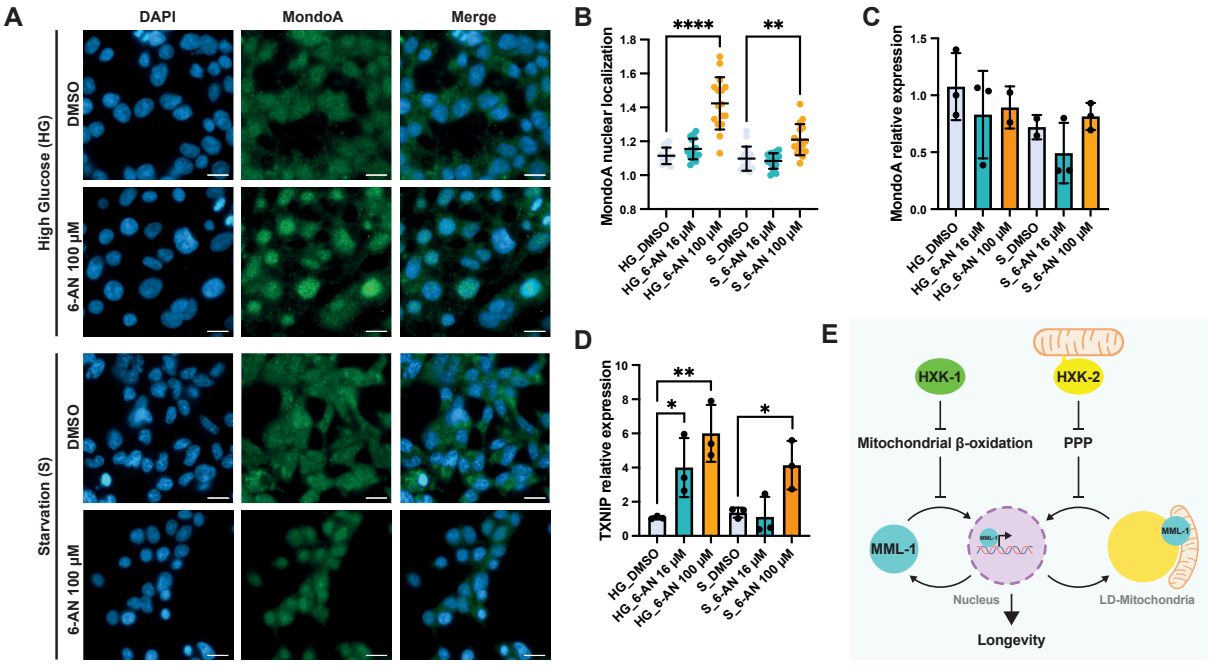

Figure 5. PPP regulates MondoA localization and transcriptional function in HEK293T cells. A. Immunofluorescence of MondoA in HEK293T cells under high glucose media (HG) and starvation (S) conditions supplemented with the PPP inhibitor 6-aminonicotinamide (6-AN) 100 μM. Scale bars, 20 μm. **B.** Quantification of MondoA nuclear localization in HEK293T cells treated with 6-AN 16 and 100 μM under HG and S conditions (N=3). **C.** Relative mRNA levels of MondoA in HEK293T cells treated with 6-AN 16 and 100 μM under HG and S conditions measured by qPCR (N=3). **D.** Relative mRNA levels of MondoA downstream target *TXNIP* in HEK293T cells treated with 6-AN 16 and 100 μM under HG and S conditions measured by qPCR (N=3). Statistical significance was calculated with one-way ANOVA in **B-D**. **B** bars represent mean ± SD, **C-D** bars represent mean ± SEM. **E.** Working model of MML-1 regulation by hexokinases. HXK-1 and HXK-2 positively regulate MML-1 through different downstream mechanisms. On the one hand, mitochondrial β-oxidation inhibition rescues MML-1 nuclear localization upon *hxk-1i*. On the other hand, the PPP regulates MML-1 subcellular localization between LD-mitochondria and the nucleus under *hxk-2i*, which is required for the lifespan extension mediated by germ-line loss. PPP, pentose phosphate pathway; LD, lipid droplet.

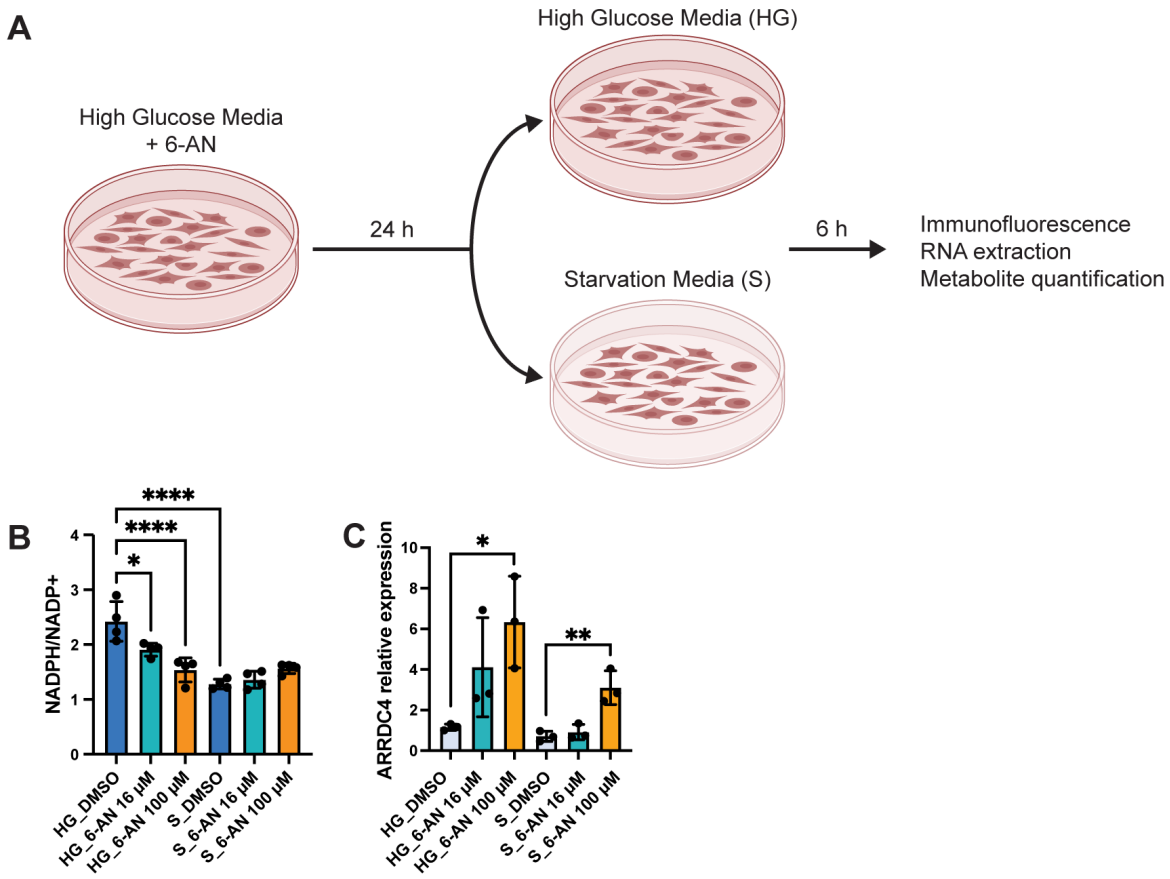

Supplementary Figure 5. Inhibition of PPP NADPH-producing enzymes by 6-AN induces MondoA downstream targets. A. Experimental design for inhibition of the PPP in HEK293T cells. Cells were grown in high glucose media (HG) supplemented with 6-AN for 24 h, and then the media was replaced with either HG or starvation (S) media for 6 h. Cells were collected for immunostaining, RNA extraction, and metabolite quantification. **B.** Quantification of $NADP^+$ and NADPH levels in HEK293T cells treated with 6-AN 16 and 100 µM under HG and S conditions (N=3). **C.** Relative mRNA levels of MondoA downstream target *ARRDC4* in HEK293T cells treated with 6-AN 16 and 100 µM under HG and S conditions measured by qPCR (N=3). Statistical significance was calculated with one-way ANOVA in **B-C**. **B-C** bars represent mean ± SEM.

References

Benhamed, F., Denechaud, P. D., Lemoine, M., Robichon, C., Moldes, M., Bertrand-Michel, J., Ratziu, V., Serfaty, L., Housset, C., Capeau, J., Girard, J., Guillou, H., & Postic, C. (2012). The lipogenic transcription factor ChREBP dissociates hepatic steatosis from insulin resistance in mice and humans. *Journal of Clinical Investigation*, *122*(6), 2176–2194. https://doi.org/10.1172/JCI41636

Bennett, C. F., Kwon, J. J., Chen, C., Russell, J., Acosta, K., Burnaevskiy, N., Crane, M. M., Bitto, A., Vander Wende, H., Simko, M., Pineda, V., Rossner, R., Wasko, B. M., Choi, H., Chen, S., Park, S., Jafari, G., Sands, B., Perez Olsen, C., … Kaeberlein, M. (2017). Transaldolase inhibition impairs mitochondrial respiration and induces a starvation-like longevity response in Caenorhabditis elegans. In *PLoS Genetics* (Vol. 13, Issue 3). https://doi.org/10.1371/journal.pgen.1006695

Billin, A. N., Eilers, A. L., Coulter, K. L., Logan, J. S., & Ayer, D. E. (2000). MondoA, a Novel Basic Helix-Loop-Helix–Leucine Zipper Transcriptional Activator That Constitutes a Positive Branch of a Max-Like Network. *Molecular and Cellular Biology*, *20*(23), 8845–8854. https://doi.org/10.1128/mcb.20.23.8845-8854.2000

Bolte, S., & Cordelières, F. P. (2006). A guided tour into subcellular colocalization analysis in light microscopy. *Journal of Microscopy*, *224*(3), 213–232. https://doi.org/10.1111/j.1365-2818.2006.01706.x

Boutant, M., Kulkarni, S. S., Joffraud, M., Ratajczak, J., Valera-Alberni, M., Combe, R., Zorzano, A., & Cantó, C. (2017). Mfn2 is critical for brown adipose tissue thermogenic function. *The EMBO Journal*, *36*(11), 1543–1558. https://doi.org/10.15252/embj.201694914

Bricker, D. K., Taylor, E. B., Schell, J. C., Orsak, T., Boutron, A., Chen, Y.-C., Cox, J. E., Cardon, C. M., Van Vranken, J. G., Dephoure, N., Redin, C., Boudina, S., Gygi, S. P., Brivet, M., Thummel, C. S., & Rutter, J. (2012). A Mitochondrial Pyruvate Carrier Required for Pyruvate Uptake in Yeast, Drosophila, and Humans. *Science*, *337*(July), 96–100. https://doi.org/10.1126/science.1218099

Carroll, P. A., Diolaiti, D., McFerrin, L., Gu, H., Djukovic, D., Du, J., Cheng, P. F., Anderson, S., Ulrich, M., Hurley, J. B., Raftery, D., Ayer, D. E., & Eisenman, R. N. (2015). Deregulated Myc Requires MondoA/Mlx for Metabolic Reprogramming and Tumorigenesis. *Cancer Cell*, *27*(2), 271–285. https://doi.org/10.1016/j.ccell.2014.11.024

Cha-Molstad, H., Saxena, G., Chen, J., & Shalev, A. (2009). Glucose-stimulated expression of Txnip is mediated by carbohydrate response element-binding protein, p300, and histone H4 acetylation in pancreatic beta cells. *Journal of Biological Chemistry*, *284*(25), 16898–16905. https://doi.org/10.1074/jbc.M109.010504

Chi, M. M. Y., Pusateri, M. E., Carter, J. G., Norris, B. J., McDougal, D. B., & Lowry, O. H. (1987). Enzymatic assays for 2-deoxyglucose and 2-deoxyglucose 6-phosphate. *Analytical Biochemistry*, *161*(2), 508–513. https://doi.org/10.1016/0003-2697(87)90481-7

1146 Chin, R. M., Fu, X., Pai, M. Y., Vergnes, L., Hwang, H., Deng, G., Diep, S., Lomenick, B.,
1147 Meli, V. S., Monsalve, G. C., Hu, E., Whelan, S. A., Wang, J. X., Jung, G., Solis, G. M.,
1148 Fazlollahi, F., Kaweeteerawat, C., Quach, A., Nili, M., … Huang, J. (2014). The
1149 metabolite α-ketoglutarate extends lifespan by inhibiting ATP synthase and TOR.
1150 *Nature*, *510*(7505), 397–401. https://doi.org/10.1038/nature13264
1151 Clancy, D. J., Gems, D., Harshman, L. G., Oldham, S., Stocker, H., Hafen, E., Leevers, S. J.,
1152 & Partridge, L. (2001). Extension of life-span by loss of CHICO, a Drosophila insulin
1153 receptor substrate protein. *Science*, *292*(5514), 104–106.
1154 https://doi.org/10.1126/science.1057991
1155 Cox, J., Hein, M. Y., Luber, C. A., Paron, I., Nagaraj, N., & Mann, M. (2014). Accurate
1156 proteome-wide label-free quantification by delayed normalization and maximal peptide
1157 ratio extraction, termed MaxLFQ. *Molecular and Cellular Proteomics*, *13*(9), 2513–
1158 2526. https://doi.org/10.1074/mcp.M113.031591
1159 Cox, J., & Mann, M. (2008). MaxQuant enables high peptide identification rates,
1160 individualized p.p.b.-range mass accuracies and proteome-wide protein quantification.
1161 *Nature Biotechnology*, *26*(12), 1367–1372. https://doi.org/10.1038/nbt.1511
1162 Dalziel, K., & Londesborough, J. C. (1968). The mechanisms of reductive carboxylation
1163 reactions: Carbon dioxide or bicarbonate as substrate of nicotinamide-adenine
1164 dinucleotide phosphate-linked isocitrate dehydrogenase and malic enzyme. *The*
1165 *Biochemical Journal*, *110*(2), 223–230. https://doi.org/10.1042/bj1100223
1166 Denechaud, P. D., Dentin, R., Girard, J., & Postic, C. (2008). Role of ChREBP in hepatic
1167 steatosis and insulin resistance. *FEBS Letters*, *582*(1), 68–73.
1168 https://doi.org/10.1016/j.febslet.2007.07.084
1169 Du, S., & Zheng, H. (2021). Role of FoxO transcription factors in aging and age-related
1170 metabolic and neurodegenerative diseases. *Cell and Bioscience*, *11*(1), 1–17.
1171 https://doi.org/10.1186/s13578-021-00700-7
1172 Fischer, F., Grigolon, G., Benner, C., & Ristow, M. (2022). Evolutionarily Conserved
1173 Transcription Factors As Regulators of Longevity and Targets for Geroprotection.
1174 *Physiological Reviews*, *102*(3), 1449–1494. https://doi.org/10.1152/physrev.00017.2021
1175 Gerisch, B., & Antebi, A. (2004). Hormonal signals produced by DAF-9/cytochrome P450
1176 regulate C. elegans dauer diapause in response to environmental cues. *Development*,
1177 *131*(8), 1765–1776. https://doi.org/10.1242/dev.01068
1178 Gerisch, B., Weitzel, C., Kober-Eisermann, C., Rottiers, V., & Antebi, A. (2001). A
1179 Hormonal Signaling Pathway Influencing C. elegans Metabolism, Reproductive

1180 Development, and Life Span. *Developmental Cell*, *1*(6), 841–851.
1181 https://doi.org/10.1016/S1534-5807(01)00085-5
1182 Ghasemi, A., Aghajani, H., Fallah, S., Assadi, M., & Seifi, M. (2015). C771G (His241Gln)
1183 polymorphism of MLXIPL Gene, TG levels and coronary artery disease: A case control
1184 study. *Anatolian Journal of Cardiology*, *15*(1), 8–12.
1185 https://doi.org/10.5152/akd.2014.5135
1186 Gordaliza-Alaguero, I., Cantó, C., & Zorzano, A. (2019). Metabolic implications of
1187 organelle–mitochondria communication. *EMBO Reports*, *20*(9), 1–27.
1188 https://doi.org/10.15252/embr.201947928
1189 Gottlob, K., Majewski, N., Kennedy, S., Kandel, E., Robey, R. B., & Hay, N. (2001).
1190 Inhibition of early apoptotic events by Akt/PKB is dependent on the first committed step
1191 of glycolysis and mitochondrial hexokinase. *Genes and Development*, *15*(11), 1406–
1192 1418. https://doi.org/10.1101/gad.889901
1193 Green, C. L., Lamming, D. W., & Fontana, L. (2021). Molecular mechanisms of dietary
1194 restriction promoting health and longevity. *Nature Reviews Molecular Cell Biology*,
1195 *0123456789*. https://doi.org/10.1038/s41580-021-00411-4
1196 Hutter, H., & Suh, J. (2016). GExplore 1.4: An expanded web interface for queries on
1197 Caenorhabditis elegans protein and gene function . *Worm*, *5*(4), e1234659.
1198 https://doi.org/10.1080/21624054.2016.1234659
1199 Iizuka, K., Miller, B., & Uyeda, K. (2006). Deficiency of carbohydrate-activated
1200 transcription factor ChREBP prevents obesity and improves plasma glucose control in
1201 leptin-deficient (ob/ob) mice. *American Journal of Physiology - Endocrinology and*
1202 *Metabolism*, *291*(2), 358–364. https://doi.org/10.1152/ajpendo.00027.2006
1203 Ishii, S., Iizuka, K., Miller, B. C., & Uyeda, K. (2004). Carbohydrate response element
1204 binding protein directly promotes lipogenic enzyme gene transcription. *Proceedings of*
1205 *the National Academy of Sciences of the United States of America*, *101*(44), 15597–
1206 15602. https://doi.org/10.1073/pnas.0405238101
1207 John, S., Weiss, J. N., & Ribalet, B. (2011). Subcellular localization of hexokinases I and II
1208 directs the metabolic fate of glucose. *PLoS ONE*, *6*(3).
1209 https://doi.org/10.1371/journal.pone.0017674
1210 Johnson, D. W., Llop, J. R., Farrell, S. F., Yuan, J., Stolzenburg, L. R., & Samuelson, A. V.
1211 (2014). The Caenorhabditis elegans Myc-Mondo/Mad Complexes Integrate Diverse
1212 Longevity Signals. *PLoS Genetics*, *10*(4). https://doi.org/10.1371/journal.pgen.1004278
1213 Ju, H. Q., Lin, J. F., Tian, T., Xie, D., & Xu, R. H. (2020). NADPH homeostasis in cancer:

1214 functions, mechanisms and therapeutic implications. *Signal Transduction and Targeted*
1215 *Therapy*, *5*(1), 1–12. https://doi.org/10.1038/s41392-020-00326-0
1216 Kaadige, M. R., Looper, R. E., Kamalanaadhan, S., & Ayer, D. E. (2009). Glutamine-
1217 dependent anapleurosis dictates glucose uptake and cell growth by regulating MondoA
1218 transcriptional activity. *Proceedings of the National Academy of Sciences of the United*
1219 *States of America*, *106*(35), 14878–14883. https://doi.org/10.1073/pnas.0901221106
1220 Kamath, R. S., & Ahringer, J. (2003). Genome-wide RNAi screening in Caenorhabditis
1221 elegans. *Methods*, *30*(4), 313–321. https://doi.org/10.1016/S1046-2023(03)00050-1
1222 Kennedy, B. K., & Lamming, D. W. (2016). The Mechanistic Target of Rapamycin: The
1223 Grand ConducTOR of Metabolism and Aging. *Cell Metabolism*, *23*(6), 990–1003.
1224 https://doi.org/10.1016/j.cmet.2016.05.009
1225 Koopman, M., Michels, H., Dancy, B. M., Kamble, R., Mouchiroud, L., Auwerx, J., Nollen,
1226 E. A. A., & Houtkooper, R. H. (2016). A screening-based platform for the assessment of
1227 cellular respiration in Caenorhabditis elegans. *Nature Protocols*, *11*(10), 1798–1816.
1228 https://doi.org/10.1038/nprot.2016.106
1229 Krahmer, N., Najafi, B., Schueder, F., Quagliarini, F., Steger, M., Seitz, S., Kasper, R.,
1230 Salinas, F., Cox, J., Uhlenhaut, N. H., Walther, T. C., Jungmann, R., Zeigerer, A.,
1231 Borner, G. H. H., & Mann, M. (2018). Organellar Proteomics and Phospho-Proteomics
1232 Reveal Subcellular Reorganization in Diet-Induced Hepatic Steatosis. *Developmental*
1233 *Cell*, *47*(2), 205-221.e7. https://doi.org/10.1016/j.devcel.2018.09.017
1234 Lapierre, L. R., De Magalhaes Filho, C. D., McQuary, P. R., Chu, C. C., Visvikis, O., Chang,
1235 J. T., Gelino, S., Ong, B., Davis, A. E., Irazoqui, J. E., Dillin, A., & Hansen, M. (2013).
1236 The TFEB orthologue HLH-30 regulates autophagy and modulates longevity in
1237 Caenorhabditis elegans. *Nature Communications*, *4*.
1238 https://doi.org/10.1038/ncomms3267
1239 Lee, S.-J., Murphy, C.T., & Kenyon, C. (2009). Glucose Shortens the Lifespan of
1240 *Caenorhabditis elegans* by Down-Regulating Aquaporin Gene Expression. *Cell*
1241 *Metabolism, 10*(5), 379-391. https://doi.org/10.1016/j.cmet.2009.10.003
1242 Lee, J. H., Kong, J., Jang, J. Y., Han, J. S., Ji, Y., Lee, J., & Kim, J. B. (2014). Lipid Droplet
1243 Protein LID-1 Mediates ATGL-1-Dependent Lipolysis during Fasting in Caenorhabditis
1244 elegans. *Molecular and Cellular Biology*, *34*(22), 4165–4176.
1245 https://doi.org/10.1128/mcb.00722-14
1246 Leigh-Brown, S., Enriquez, J. A., & Odom, D. T. (2010). Nuclear transcription factors in
1247 mammalian mitochondria. *Genome Biology*, *11*(7), 1–9. https://doi.org/10.1186/gb-

2010-11-7-215

Li, F., Wang, Y., Zeller, K. I., Potter, J. J., Wonsey, D. R., O'Donnell, K. A., Kim, J., Yustein, J. T., Lee, L. A., & Dang, C. V. (2005). Myc Stimulates Nuclearly Encoded Mitochondrial Genes and Mitochondrial Biogenesis. *Molecular and Cellular Biology*, *25*(14), 6225–6234. https://doi.org/10.1128/mcb.25.14.6225-6234.2005

Lindén, M., Gellerfors, P., & Dean Nelson, B. (1982). Pore protein and the hexokinase-binding protein from the outer membrane of rat liver mitochondria are identical. *FEBS Letters*, *141*(2), 189–192. https://doi.org/10.1016/0014-5793(82)80044-6

Ma, L., Robinson, L. N., & Towle, H. C. (2006). ChREBP·Mlx is the principal mediator of glucose-induced gene expression in the liver. *Journal of Biological Chemistry*, *281*(39), 28721–28730. https://doi.org/10.1074/jbc.M601576200

Marchenko, N. D., Wolff, S., Erster, S., Becker, K., & Moll, U. M. (2007). Monoubiquitylation promotes mitochondrial p53 translocation. *EMBO Journal*, *26*(4), 923–934. https://doi.org/10.1038/sj.emboj.7601560

Marinov, G. K., Wang, Y. E., Chan, D., & Wold, B. J. (2014). Evidence for site-specific occupancy of the mitochondrial genome by nuclear transcription factors. *PLoS ONE*, *9*(1), 1–24. https://doi.org/10.1371/journal.pone.0084713

Massari, M. E., & Murre, C. (2000). *Helix-Loop-Helix Proteins: Regulators of Transcription in Eucaryotic*. *20*(2), 429–440. https://doi.org/10.1128/mcb.20.2.429-440.2000

Mejhert, N., Kuruvilla, L., Gabriel, K. R., Elliott, S. D., Guie, M. A., Wang, H., Lai, Z. W., Lane, E. A., Christiano, R., Danial, N. N., Farese, R. V., & Walther, T. C. (2020). Partitioning of MLX-Family Transcription Factors to Lipid Droplets Regulates Metabolic Gene Expression. *Molecular Cell*, *77*(6), 1251-1264.e9. https://doi.org/10.1016/j.molcel.2020.01.014

Motola, D. L., Cummins, C. L., Rottiers, V., Sharma, K. K., Li, T., Li, Y., Suino-Powell, K., Xu, H. E., Auchus, R. J., Antebi, A., & Mangelsdorf, D. J. (2006). Identification of Ligands for DAF-12 that Govern Dauer Formation and Reproduction in C. elegans. *Cell*, *124*(6), 1209–1223. https://doi.org/10.1016/j.cell.2006.01.037

Mutlu, A. S., Gao, S. M., Zhang, H., & Wang, M. C. (2020). Olfactory specificity regulates lipid metabolism through neuroendocrine signaling in Caenorhabditis elegans. *Nature Communications*, *11*(1), 1–15. https://doi.org/10.1038/s41467-020-15296-8

Nakamura, S., Karalay, Ö., Jäger, P. S., Horikawa, M., Klein, C., Nakamura, K., Latza, C., Templer, S. E., Dieterich, C., & Antebi, A. (2016). Mondo complexes regulate TFEB via TOR inhibition to promote longevity in response to gonadal signals. *Nature*

Communications, *7*. https://doi.org/10.1038/ncomms10944

Orlandi, I., Coppola, D. P., & Vai, M. (2014). Rewiring yeast acetate metabolism through mpc1 loss of function leads to mitochondrial damage and decreases chronological lifespan. *Microbial Cell*, *1*(12), 393–405. https://doi.org/10.15698/mic2014.12.178

Owen, O. E., Kalhan, S. C., & Hanson, R. W. (2002). The key role of anaplerosis and cataplerosis for citric acid cycle function. *Journal of Biological Chemistry*, *277*(34), 30409–30412. https://doi.org/10.1074/jbc.R200006200

Papsdorf, K., Miklas, J. W., Hosseini, A., Cabruja, M., Morrow, C. S., Savini, M., Yu, Y., Silva-garcía, C. G., Haseley, N. R., Murphy, L. M., Yao, P., Launoit, E. De, Dixon, S. J., Snyder, M. P., Wang, M. C., Mair, W. B., & Brunet, A. (2023). Lipid droplets and peroxisomes are co-regulated to drive lifespan extension in response to mono-unsaturated fatty acids. *Nature Cell Biology*. https://doi.org/10.1038/s41556-023-01136-6

Pastorino, J. G., Shulga, N., & Hoek, J. B. (2002). Mitochondrial binding of hexokinase II inhibits Bax-induced cytochrome c release and apoptosis. *Journal of Biological Chemistry*, *277*(9), 7610–7618. https://doi.org/10.1074/jbc.M109950200

Penkov, S., Kaptan, D., Erkut, C., Sarov, M., Mende, F., & Kurzchalia, T. V. (2015). Integration of carbohydrate metabolism and redox state controls dauer larva formation in Caenorhabditis elegans. *Nature Communications*, *6*. https://doi.org/10.1038/ncomms9060

Pickett, C. L., Breen, K. T., & Ayer, D. E. (2007). A C. elegans Myc-like network cooperates with semaphorin and Wnt signaling pathways to control cell migration. *Developmental Biology*, *310*(2), 226–239. https://doi.org/10.1016/j.ydbio.2007.07.034

Postic, C., Dentin, R., Denechaud, P. D., & Girard, J. (2007). ChREBP, a transcriptional regulator of glucose and lipid metabolism. *Annual Review of Nutrition*, *27*, 179–192. https://doi.org/10.1146/annurev.nutr.27.061406.093618

R Core Team. (2017). *R: A language and environment for statistical computing* (3.4.3). R Foundation for Statistical Computing. https://www.r-project.org/

Ralser, M., Wamelink, M. M., Struys, E. A., Joppich, C., Krobitsch, S., Jakobs, C., & Lehrach, H. (2008). A catabolic block does not sufficiently explain how 2-deoxy-D-glucose inhibits cell growth. *Proceedings of the National Academy of Sciences of the United States of America*, *105*(46), 17807–17811. https://doi.org/10.1073/pnas.0803090105

Ramachandran, P. V., Savini, M., Folick, A. K., Hu, K., Masand, R., Graham, B. H., &

Wang, M. C. (2019). Lysosomal Signaling Promotes Longevity by Adjusting Mitochondrial Activity. *Developmental Cell*, *48*(5), 685-696.e5. https://doi.org/10.1016/j.devcel.2018.12.022

Rambold, A. S., Cohen, S., & Lippincott-Schwartz, J. (2015). Fatty acid trafficking in starved cells: Regulation by lipid droplet lipolysis, autophagy, and mitochondrial fusion dynamics. *Developmental Cell*, *32*(6), 678–692. https://doi.org/10.1016/j.devcel.2015.01.029

Ratnappan, R., Amrit, F.R.G., Chen, S.-W., Gill, H., Ward, J., Yamamoto, K.R., Olse, C.P., & Ghazi, A. (2014). Germline signals deploy NHR-49 to modulate fatty-acid β-oxidation and desaturation in somatic tissues of *C. elegans*. *PLoS Genetics*, *10*(12), e1004829. https://doi.org/10.1371/journal.pgen.1004829.

Richards, P., Ourabah, S., Montagne, J., Burnol, A. F., Postic, C., & Guilmeau, S. (2017). MondoA/ChREBP: The usual suspects of transcriptional glucose sensing; Implication in pathophysiology. *Metabolism: Clinical and Experimental*, *70*, 133–151. https://doi.org/10.1016/j.metabol.2017.01.033

Ritchie, M. E., Phipson, B., Wu, D., Hu, Y., Law, C. W., Shi, W., & Smyth, G. K. (2015). limma powers differential expression analyses for RNA-sequencing and microarray studies. *Nucleic Acids Research*, *43*(7), e47. https://doi.org/10.1093/nar/gkv007

Roberts, D. J., Tan-Sah, V. P., Ding, E. Y., Smith, J. M., & Miyamoto, S. (2014). Hexokinase-II Positively Regulates Glucose Starvation-Induced Autophagy through TORC1 Inhibition. *Molecular Cell*, *53*(4), 521–533. https://doi.org/10.1016/j.molcel.2013.12.019

Rual, J. F., Ceron, J., Koreth, J., Hao, T., Nicot, A. S., Hirozane-Kishikawa, T., Vandenhaute, J., Orkin, S. H., Hill, D. E., van den Heuvel, S., & Vidal, M. (2004). Toward improving Caenorhabditis elegans phenome mapping with an ORFeome-based RNAi library. *Genome Research*, *14*(10 B), 2162–2168. https://doi.org/10.1101/gr.2505604

Sans, C. L., Satterwhite, D. J., Stoltzman, C. A., Breen, K. T., & Ayer, D. E. (2006). MondoA-Mlx Heterodimers Are Candidate Sensors of Cellular Energy Status: Mitochondrial Localization and Direct Regulation of Glycolysis. *Molecular and Cellular Biology*, *26*(13), 4863–4871. https://doi.org/10.1128/mcb.00657-05

Schulz, T.J., Zarse, K., Voigt, A., Urban, N., Birringer, M., & Ristow, M. (2007). Glucose Restriction Extends *Caenorhabditis elegans* Life Span by Inducing Mitochondrial Respiration and Increasing Oxidative Stress. *Cell Metabolism*, *6*(4), 280-293.

https://doi.org/10.1016/j.cmet.2007.08.011

Selman, C., Lingard, S., Choudhury, A. I., Batterham, R. L., Claret, M., Clements, M., Ramadani, F., Okkenhaug, K., Schuster, E., Blanc, E., Piper, M. D., Al-Qassab, H., Speakman, J. R., Carmignac, D., Robinson, I. C. A., Thornton, J. M., Gems, D., Partridge, L., & Withers, D. J. (2008). Evidence for lifespan extension and delayed age–related biomarkers in insulin receptor substrate 1 null mice. *The FASEB Journal*, *22*(3), 807–818. https://doi.org/10.1096/fj.07-9261com

Stoltzman, C. A., Kaadige, M. R., Peterson, C. W., & Ayer, D. E. (2011). MondoA senses non-glucose sugars: Regulation of thioredoxin-interacting protein (TXNIP) and the hexose transport curb. *Journal of Biological Chemistry*, *286*(44), 38027–38034. https://doi.org/10.1074/jbc.M111.275503

Stoltzman, C. A., Peterson, C. W., Breen, K. T., Muoio, D. M., Billin, A. N., & Ayer, D. E. (2008). Glucose sensing by MondoA:Mlx complexes: A role for hexokinases and direct regulation of thioredoxin-interacting protein expression. *Proceedings of the National Academy of Sciences of the United States of America*, *105*(19), 6912–6917. https://doi.org/10.1073/pnas.0712199105

Sui, D., & Wilson, J. E. (1997). Structural determinants for the intracellular localization of the isozymes of mammalian hexokinase: Intracellular localization of fusion constructs incorporating structural elements from the hexokinase isozymes and the green fluorescent protein. *Archives of Biochemistry and Biophysics*, *345*(1), 111–125. https://doi.org/10.1006/abbi.1997.0241

Tatenaka, Y., Kato, H., Ishiyama, M., Sasamoto, K., Shiga, M., Nishitoh, H., & Ueno, Y. (2019). Monitoring Lipid Droplet Dynamics in Living Cells by Using Fluorescent Probes. *Biochemistry*, *58*(6), 499–503. https://doi.org/10.1021/acs.biochem.8b01071

Tong, X., Zhao, F., Mancuso, A., Gruber, J. J., & Thompson, C. B. (2009). The glucose-responsive transcription factor ChREBP contributes to glucose-dependent anabolic synthesis and cell proliferation. *Proceedings of the National Academy of Sciences of the United States of America*, *106*(51), 21660–21665. https://doi.org/10.1073/pnas.0911316106

Van Gilst, M. R., Hadjivassiliou, H., & Yamamoto, K. R. (2005). A Caenorhabditis elegans nutrient response system partially dependent on nuclear receptor NHR-49. *Proceedings of the National Academy of Sciences of the United States of America*, *102*(38), 13496–13501. https://doi.org/10.1073/pnas.0506234102

Vrablik, T. L., Petyuk, V. A., Larson, E. M., Smith, R. D., & Watts, J. L. (2015). Lipidomic

and proteomic analysis of Caenorhabditis elegans lipid droplets and identification of ACS-4 as a lipid droplet-associated protein. *Biochimica et Biophysica Acta - Molecular and Cell Biology of Lipids*, *1851*(10), 1337–1345. https://doi.org/10.1016/j.bbalip.2015.06.004

Wang, M. C., O'Rourke, E. J., & Ruvkun, G. (2008). Fat metabolism links germline stem cells and longevity in C. elegans. *Science*, *322*(5903), 957–960. https://doi.org/10.1126/science.1162011

Wilde, B. R., Ye, Z., Lim, T. Y., & Ayer, D. E. (2019). Cellular acidosis triggers human mondoa transcriptional activity by driving mitochondrial atp production. *ELife*, *8*, 1–25. https://doi.org/10.7554/eLife.40199

Wilson, J. E. (2003). Isozymes of mammalian hexokinase: Structure, subcellular localization and metabolic function. *Journal of Experimental Biology*, *206*(12), 2049–2057. https://doi.org/10.1242/jeb.00241

Wolf, A. J., Reyes, C. N., Liang, W., Becker, C., Shimada, K., Wheeler, M. L., Cho, H. C., Popescu, N. I., Coggeshall, K. M., Arditi, M., & Underhill, D. M. (2016). Hexokinase Is an Innate Immune Receptor for the Detection of Bacterial Peptidoglycan. *Cell*, *166*(3), 624–636. https://doi.org/10.1016/j.cell.2016.05.076

Yamamoto-Imoto, H., Minami, S., Shioda, T., Yamashita, Y., Sakai, S., Maeda, S., Yamamoto, T., Oki, S., Takashima, M., Yamamuro, T., Yanagawa, K., Edahiro, R., Iwatani, M., So, M., Tokumura, A., Abe, T., Imamura, R., Nonomura, N., Okada, Y., … Yoshimori, T. (2022). Age-associated decline of MondoA drives cellular senescence through impaired autophagy and mitochondrial homeostasis. *Cell Reports*, *38*(9), 110444. https://doi.org/10.1016/j.celrep.2022.110444

Yamashita, H., Takenoshita, M., Sakurai, M., Bruick, R. K., Henzel, W. J., Shillinglaw, W., Arnot, D., & Uyeda, K. (2001). A glucose-responsive transcription factor that regulates carbohydrate metabolism in the liver. *Proceedings of the National Academy of Sciences of the United States of America*, *98*(16), 9116–9121. https://doi.org/10.1073/pnas.161284298

Yamawaki, T. M., Berman, J. R., Suchanek-Kavipurapu, M., McCormick, M., Gaglia, M. M., Lee, S. J., & Kenyon, C. (2010). The somatic reproductive tissues of C. elegans promote longevity through steroid hormone signaling. *PLoS Biology*, *8*(8), 45–46. https://doi.org/10.1371/journal.pbio.1000468

Zhang, Y., Lanjuin, A., Chowdhury, S. R., Mistry, M., Silva-García, C. G., Weir, H. J., Chia-Lin, L., Escoubas, C. C., Tabakovic, E., & Mair, W. B. (2019). Neuronal TORC1

modulates longevity via ampk and cell nonautonomous regulation of mitochondrial dynamics in C. Elegans. *ELife*, *8*, 1–24. https://doi.org/10.7554/eLife.49158